

Chapter 5

Testing post-Newtonian theory with gravitational wave observations

5.1 Introduction

Ever since the formulation of general relativity (GR), there have been many proposals to test its predictions. Most important of them are the solar system tests and tests using binary pulsars [192]. The binary pulsar test provides one of the most stringent tests of gravity in the strong field regime of GR and its alternatives [193]. The *direct* detection of gravitational waves, one of the most fundamental predictions of GR, will only be a test of the relativistic nature of gravity. Since any relativistic theory of gravitation, not necessarily GR, predicts radiative solutions of the field equations, one has to be careful in interpreting the detection in favour of any theory.

Post-Newtonian theory has been highly successful in explaining the decay of the orbital period in binary pulsars and in confirming the emission of gravitational radiation by these relativistic systems (cf. [194] and references therein). Nevertheless, the binary pulsar radio observations do not test PN theory to a high order. This is because the typical velocity in the most relativistic of binary pulsars is $v/c \approx 3 \times 10^{-3}$, which is not large enough for higher order terms to be important.

GW observations of the coalescence of binary black holes (BBH) will provide a unique opportunity to test PN theory to very high orders. This is because the velocities in the system, close to the merger, could be as high as $v/c \approx 0.2-0.4$, making the highest order known PN term $10^{12}-10^{14}$ times more important for GW observations than for radio binary pulsars. Several tests of general relativity have already been proposed by various authors [167, 195, 196].

The possibility of using GW observations to discriminate GR from other theories of grav-

ity such as Brans-Dicke (BD) theory or massive graviton theory, has been studied exhaustively by Will and his collaborators [196]. BD theory is a scalar tensor theory which, unlike GR, predicts dipole GWs. Using ground-based detectors Ref. [197] examined the possibility of testing the dipole term in the phasing formula and bounds that can be put on the BD coupling parameter ω_{BD} . The bound, as they found, can be as high as 2000 which is about four times higher than that possible with solar system measurements. The bounds that are possible with future space-based experiments such as LISA were examined in Ref. [198]. The bound with LISA may be as high as 240,000. For testing BD theory, the suitable systems are those whose mass ratio is small; typically a NS spiralling into a **massive/intermediate mass/supermassive** BH where the effect of the coupling term is most dominant.

Another possible theory of gravity is the theory of the massive graviton where Compton wavelength λ_g of graviton is not infinite as in GR. Bounds can be placed on λ_g from GW observations. With the ground-based detector the bound is about 2×10^{12} km [195] (for an equal mass binary BH of $10M_\odot$). Space based experiments would place a more stringent bound on it, which may be about 7×10^{12} km [195] (by the observation of inspiral of a SMBH binary of 10^6M_\odot each). The calculation in the above mentioned work used the λ_g -dependent term which occurs at 1PN in the phasing formula. A critical paper by Damour and Esposito-Farèse contrasted the subtleties involved in interpreting the results in the case of GW observations against those in the binary pulsar case [199]. These should be kept in mind while assessing the works discussed above. The possibility to set up these tests is based on being able to estimate the parameters of the source by GW observations. We begin by reviewing the basic elements of parameter estimation to the extent we require in the following section.

5.2 Phasing formula

In a black hole binary, as the two holes orbit about their **centre-of-mass**, the energy and angular momentum from the system is dissipated into gravitational radiation. The radiation back-reaction force causes the two bodies to gradually spiral in towards each other, resulting in a strong burst of radiation just before they merge to form a single black hole. The radiation emitted at the end of the binary evolution is the primary target of both the **ground-** and **space-**based interferometric gravitational wave (GW) antennas [33]. It has become necessary to gain an accurate understanding of the late-time evolution of binaries in order to help data analysts in detecting the signal and measuring the parameters by fitting the observed signal with that expected from general relativity.

In the general theory of relativity there is no exact solution to the two-body problem. In the absence of an exact solution (analytical or numerical) theorists have resorted to an

approximate solution to the problem using post-Newtonian (PN) theory. Briefly, the programme of PN theory is the following. Let us consider a binary consisting of two **non-spinning** black holes of masses m_1 and m_2 (total mass $M = m_1 + m_2$, symmetric mass ratio $\nu = m_1 m_2 / M^2$) separated by an orbital (Schwarzschild coordinate) distance $r(t)$. Post-Newtonian theory expresses the relevant physical quantities as a series in the 'small' velocity parameter $\epsilon = v/c \equiv \sqrt{GM/rc^2}$. For a system consisting of non-spinning black holes the only relevant quantities are the (specific) binding energy E and the GW flux \mathcal{F} , which are obtained as perturbative expansions in v . Following the standard convention, in units where $G = c = 1$, v^n corresponds to a term of order $\frac{n}{2}$ -PN. Currently, these expansions are known to order v^7 or 3.5PN [200, 108, 109, 86, 102, 89, 951]:

$$E = -\frac{1}{2} \nu v^2 \sum_{k=0}^3 E_k v^{2k}, \quad (5.1a)$$

$$\mathcal{F} = \frac{32}{5} \nu^2 v^{10} \sum_{k=0}^7 \mathcal{F}_k v^k, \quad (5.1b)$$

where E_k and \mathcal{F}_k are the PN expansion coefficients that are all functions of the dimensionless mass ratio $\nu = m_1 m_2 / M^2$. Here $M = m_1 + m_2$ is the total mass of the binary. (Though for this schematic presentation we write above a Taylor-expansion in v^k , recall that there are also $\log v$ in the expansion.)

In the adiabatic approximation one then uses the energy balance equation, $-dE/dt = \mathcal{F}$, to compute the evolution of the orbital phase $\varphi(t)$ using the following coupled ordinary differential equations:

$$\frac{d\varphi}{dt} = \omega = \frac{v^3}{M}, \quad (5.2a)$$

$$\frac{dv}{dt} = \frac{dE/dt}{dE/dv} = \frac{-\mathcal{F}}{E'(v)}, \quad (5.2b)$$

where $E'(v) \equiv dE/dv$. The phase $\Phi(t)$ of the emitted radiation at dominant order is simply twice the orbital phase: $\Phi(t) = 2\varphi(t)$.

The phasing formula obtained by solving the above differential equations includes different PN terms arising from nonlinear multipole interactions as the wave propagates from the source's near-zone to the far-zone [63, 145, 158]. As discussed in Chapter 1 the 1.5PN and 2.5PN terms arise solely due to the interaction of the Amowitt-Deser-Misner (ADM) mass of the source and the quadrupole moment. It is physically due to the scattering of **quadrupolar** waves off the Schwarzschild curvature generated by the source and is referred to as the gravitational wave tail. The 3PN term includes, in addition to the terms at the retarded time,

¹In this chapter and the next in some of the formulas the dependence on c is indicated for convenience, even though for consistency those c 's should be set equal to one in the numerical calculations.

more interestingly the cubic nonlinear interactions due to the scattering of the wave tails by the ADM mass energy of the spacetime. The observational tests of these PN terms in effect test the nonlinear structure of Einstein's gravity.

In the restricted PN approximation (so called because one keeps only the PN corrections to the phase of the radiation but neglects the PN corrections in the amplitude), the response of an interferometric antenna to the incident radiation from a source at a luminosity distance D_L is

$$h(t) = \frac{4CM}{D_L} [\pi MF(t)]^{2/3} \cos \Phi(t), \quad (5.3)$$

where $M = \nu^{3/5} \mathcal{M}$ is the so-called *chirp* mass of the system. In the above, \mathcal{M} and M are the observed chirp and total masses. They are related to masses measured in the source rest frame by

$$\mathcal{M} = (1+z)M_{\text{source}}, \quad M = (1+z)M_{\text{source}}, \quad (5.4)$$

where z is the cosmological redshift. Further, $F(t) \equiv \frac{1}{2\pi} \frac{d\Phi(t)}{dt}$ is the instantaneous frequency of the radiation, $0 \leq C \leq 1$ is a dimensionless geometric factor that depends on the relative orientation of the binary and the detector whose average over all orientations is $\bar{C} = 2/5$. The importance of including PN corrections in the phase but conveniently neglecting them in the amplitude was realized quite early on [137] and led to a lot of simplification of the data analysis problem. For the tests proposed in this chapter it may eventually be necessary to incorporate these amplitude corrections [110, 43]. For the sake of simplicity, however, we have refrained from doing so in this work.

A brief summary of the cosmological model we employ is in order. Let Ω_M be the matter (dark plus baryonic) density parameter, Ω_Λ , the cosmological constant or vacuum density parameter and Ω_κ , the density parameter associated with the curvature constant. For a zero-spatial-curvature universe $\Omega_\kappa = 0$ and matter density $\Omega_\Lambda + \Omega_M = 1$, the luminosity distance² is given by

$$D_L = \frac{c(1+z)}{H_0} \int_0^z \frac{dz'}{[\Omega_M(1+z')^3 + \Omega_\Lambda]^{1/2}}. \quad (5.5)$$

In our calculations we used $\Omega_M = 0.3$, $\Omega_\Lambda = 0.7$ and $H_0 = 70 \text{ Km/sec/Mpc}$.

For our purposes it will be useful to work with the Fourier transform of the signal $h(t)$ Eq. (5.3), which is given by

$$\tilde{h}(f) \equiv \int_{-\infty}^{\infty} h(t) \exp(2\pi i f t) dt. \quad (5.6)$$

²Luminosity distance, D_L , is a term used in astronomy to describe the distance at which an astronomical body would lie based on its observed luminosity in the absence of any unanticipated attenuation.

Using the stationary phase approximation it has been shown that [33, 201]

$$\tilde{h}(f) = \mathcal{A} f^{-7/6} \exp \left[i\Psi(f) + i\frac{\pi}{4} \right], \quad (5.7)$$

with the Fourier amplitude \mathcal{A} given by

$$\mathcal{A} = \frac{C}{D_L \pi^{2/3}} \sqrt{\frac{5}{24}} \mathcal{M}^{5/6}, \quad (5.8)$$

and phase $\Psi(v(f))$, (where $v = (n M f)^{1/3}$), given by [26, 40]:

$$\begin{aligned} \Psi(v) = & 2\pi f t_c - \Phi_c + \frac{3}{128} v^{-1} v^{-5} \left\{ 1 \right. \\ & + \left(\frac{3715}{756} + \frac{55}{9} v \right) v^2 - 16\pi v^3 \\ & + \left(\frac{15293365}{508032} + \frac{27145}{504} v + \frac{3085}{72} v^2 \right) v^4 \\ & + \pi \left(\frac{38645}{756} - \frac{65}{9} v \right) \left[1 + 3 \ln \left(\frac{v}{v_{\text{iso}}} \right) \right] v^5 \\ & + \left[\frac{11583231236531}{4694215680} - \frac{640}{3} \pi^2 - \frac{6848}{21} \gamma \right. \\ & + \left. \left(-\frac{15737765635}{3048192} + \frac{2255}{12} \pi^2 \right) v \right. \\ & + \left. \frac{76055}{1728} v^2 - \frac{127825}{1296} v^3 - \frac{6848}{189} \ln(4v) \right] v^6 \\ & + \left. \pi \left(\frac{77096675}{254016} + \frac{378515}{1512} v - \frac{74045}{756} v^2 \right) v^7 \right\}. \quad (5.9) \end{aligned}$$

Here t_c and Φ_c are the fiducial epoch of merger and the phase of the signal at that epoch. $\gamma = 0.5772156649\dots$ the Euler Gamma Function³

5.2.1 Dealing with the log terms

An examination of the above formula reveals that in addition to a polynomial dependence on v , there is also a $\log v$ dependence. This is a consequence of the fact that the post-Newtonian series is an asymptotic series in gauge functions $c^{-m}(\log c)^n$. This additional complication requires a strategy to treat that log dependence. The log-terms are treated in three different ways as discussed below:

1. Log-Constant: In this method the log terms are treated as constants with respect to the

³Note that γ denotes the Euler Gamma function and not $Gm/c^2 r$ as in the literature on the generation problem as in the earlier chapters.

frequency with the justification that the log-dependence on the frequency is weak in the relevant bandwidth. The $\Psi(f)$ in compact form then looks like

$$\Psi(f) = 2\pi f t_c + \Phi_c + \sum_k \psi_k f^{(k-5)/3} \quad (5.10)$$

The ψ_k now are given by

$$\psi_k = \frac{3}{128\nu} (\pi M)^{(k-5)/3} \alpha_k, \quad (5.11)$$

where.

$$\begin{aligned} \alpha_0 &= 1, \\ \alpha_1 &= 0, \\ \alpha_2 &= \frac{3715}{756} + \frac{55}{9}\nu, \\ \alpha_3 &= -16\pi, \\ \alpha_4 &= \frac{15293365}{508032} + \frac{27145}{504}\nu + \frac{3085}{72}\nu^2, \\ \alpha_5 &= \pi \left(\frac{38645}{756} - \frac{65}{9}\nu \right) \left[1 + \ln(6^{3/2}\pi M f) \right] \\ \alpha_6 &= \frac{11583231236531}{4694215680} - \frac{640}{3}\pi^2 - \frac{6848}{21}\gamma \\ &\quad + \left(-\frac{15737765635}{3048192} + \frac{2255}{12}\pi^2 \right) \nu \\ &\quad + \frac{76055}{1728}\nu^2 - \frac{127825}{1296}\nu^3 - \frac{6848}{63} \ln(64\pi M f), \\ \alpha_7 &= \pi \left(\frac{77096675}{254016} + \frac{378515}{1512}\nu - \frac{74045}{756}\nu^2 \right). \end{aligned} \quad (5.12)$$

2. Log-Expanded : In this method the log terms are expanded about v_{iso} which is the invariant speed at the last stable orbit during the coalescence of the binary. For a test mass in a Schwarzschild spacetime v_{iso} is equal $\frac{1}{\sqrt{6}}$. Substituting the expanded expression in the formula of $\Psi(f)$ keeping the needed terms and neglecting the terms higher than 3.5PN, the $\Psi(f)$ then becomes

$$\Psi(f) = 2\pi f t_c + \Phi_c + \sum_k \psi_k f^{(k-5)/3}. \quad (5.13)$$

The ψ_k 's are independent of f and given by

$$\psi_k = \frac{3}{128\nu} (\pi M)^{(k-5)/3} \tilde{\alpha}_k. \quad (5.14)$$

$\tilde{\alpha}_k = \alpha_k$ for $k = 0, 2, 3, 4$ and for the remaining, $\alpha_0, \alpha_1, \alpha_3$ and α_4 are as given in Eq. (5.12). For the remaining

$$\begin{aligned}\tilde{\alpha}_5 &= \pi \left(-\frac{7334821}{21168} + \frac{12337}{252} \nu \right), \\ \tilde{\alpha}_6 &= \frac{15552276814259}{4694215680} - \frac{6848}{21} \gamma + \frac{38645}{6\sqrt{6}} \pi - \frac{640}{3} \pi^2 + \frac{3424}{21} \ln\left(\frac{3}{2}\right) \\ &\quad + \left(-\frac{15737765635}{3048192} - 455\sqrt{2/3}\pi + \frac{2255}{12}\pi^2 \right) \nu + \frac{76055}{1728} \nu^2 - \frac{127825}{1296} \nu^3, \\ \tilde{\alpha}_7 &= -6848\sqrt{2/3} - \frac{2377015405}{254016} \pi + \frac{2442395}{1512} \pi \nu - \frac{74045}{756} \pi \nu^2.\end{aligned}\quad (5.15)$$

3. Independent parameters for Logs: In this choice the coefficients of the log-terms are treated as additional signal parameters. This choice indeed increases the dimensionality of the parameter space making the Fisher matrix highly ill-conditioned. The $\Psi(f)$ may be written as

$$\Psi(f) = 2\pi f t_c + \Phi_c + \sum_k [\psi_k + \psi_{kl} \ln(f)] f^{(k-5)/3}, \quad (5.16)$$

where, ψ_k and ψ_{kl} are independent of f and given by

$$\begin{aligned}\psi_k &= \frac{3}{128\nu} (\pi M)^{(k-5)/3} \tilde{\alpha}_k, \\ \psi_{kl} &= \frac{3}{128\nu} (\pi M)^{(k-5)/3} \alpha_{kl}.\end{aligned}\quad (5.17)$$

$\tilde{\alpha}_k = \alpha_k$, for $k=0, 2, 3, 4$. $\alpha_{kl} = 0$ for $k = 0, 1, 2, 3, 4$.

For the rest,

$$\begin{aligned}\tilde{\alpha}_5 &= \pi \left(\frac{38645}{756} - \frac{65}{9} \nu \right) \left[1 + \ln(6^{3/2} \pi M) \right], \\ \alpha_{5l} &= \pi \left(\frac{38645}{756} - \frac{65}{9} \nu \right), \\ \tilde{\alpha}_6 &= \frac{11583231236531}{4694215680} - \frac{640}{3} \pi^2 - \frac{6848}{21} \gamma \\ &\quad + \left(-\frac{15737765635}{3048192} + \frac{2255}{12} \pi^2 \right) \nu \\ &\quad + \frac{76055}{1728} \nu^2 - \frac{127825}{1296} \nu^3 - \frac{6848}{63} \ln(64\pi M), \\ \alpha_{6l} &= -\frac{6848}{63},\end{aligned}$$

$$\begin{aligned}\bar{\alpha}_7 &= \pi \left(\frac{77096675}{254016} + \frac{378515}{1512} \nu - \frac{74045}{756} \nu^2 \right), \\ \alpha_{71} &= 0.\end{aligned}\tag{5.18}$$

5.3 Ground-based detectors

In this section we list the noise psd and the calculation of the signal to noise ratio(SNR) of the various ground based detectors that we will employ in our analysis. These include the kilometer class GW detectors Initial LIGO and Virgo followed by the next generation american detector Advanced LIGO and finally the third generation European EGO.

5.3.1 Sensitivity curves

5.3.1.1 Initial-LIGO

The LIGO noise curve [26] is given by

$$S_h(f) = S_0 \left[\left(4.49 \frac{f}{f_0} \right)^{-56} + 0.16 \left(\frac{f}{f_0} \right)^{-4.52} + 0.52 + 0.32 \left(\frac{f}{f_0} \right)^2 \right],\tag{5.19}$$

where $f_0 = 150$ Hz , $f_s = 40$ Hz, and $S_0 = 9.00 \times 10^{-46}$ Hz⁻¹.

5.3.1.2 Virgo

The Virgo noise curve [26] is given by

$$S_h(f) = S_0 \left[\left(6.23 \frac{f}{f_0} \right)^{-5} + 2 \left(\frac{f}{f_0} \right)^{-1} + 1 + \left(\frac{f}{f_0} \right)^2 \right],\tag{5.20}$$

where $f_0 = 500$ Hz, $f_s = 20$ Hz, and $S_0 = 3.24 \times 10^{-46}$ Hz⁻¹.

5.3.1.3 Advanced-LIGO

The Advanced LIGO noise curve [202] is given by

$$\begin{aligned}S_h(f) &= S_0 \left[\left(\frac{f}{f_0} \right)^{-4.14} - 5 \left(\frac{f}{f_0} \right)^{-2} \right. \\ &\quad \left. + 111 \left(1 - \left(\frac{f}{f_0} \right)^2 + \frac{1}{2} \left(\frac{f}{f_0} \right)^4 \right) / \left(1 + \frac{1}{2} \left(\frac{f}{f_0} \right)^2 \right) \right],\end{aligned}\tag{5.21}$$

where $f_0 = 215$ Hz, $f_s = 20$ Hz, and $S_0 = 1 \times 10^{-49}$ Hz⁻¹.

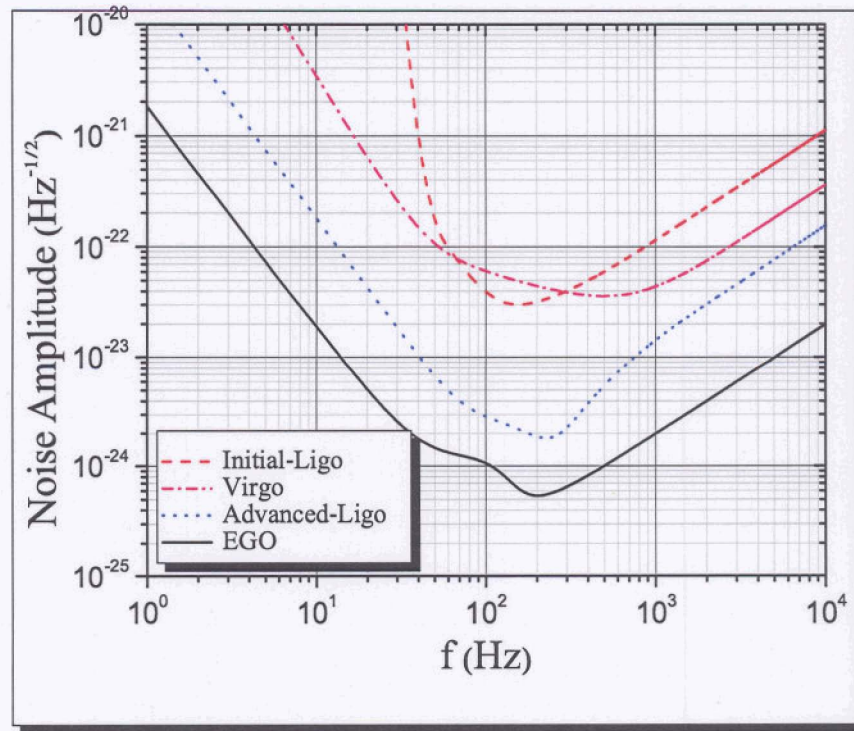


Figure 5.1: Noise amplitude plots of ground-based detectors Virgo, Initial-LIGO, Advanced-LIGO and EGO as a function of frequency f (Hz). The minima of the noise amplitude appear at the frequencies $f \equiv f_0 = \{500, 150, 215, 200\}$ Hz for $\{\text{Virgo, Initial-LIGO, Advanced-LIGO, EGO}\}$ respectively.

53.14 EGO

Finally, the EGO noise curve [203, 204] is given by

$$\begin{aligned}
 S_h(f) = & S_0 \left[\left(\frac{f}{f_0} \right)^{-4.05} + 185.62 \left(\frac{f}{f_0} \right)^{-0.69} \right. \\
 & + \left\{ 232.56 + 7251.22 \left(\frac{f}{f_0} \right)^1 - 15051.28 \left(\frac{f}{f_0} \right)^2 \right. \\
 & + 12148.93 \left(\frac{f}{f_0} \right)^3 - 9804.73 \left(\frac{f}{f_0} \right)^4 + 2365.1352 \left(\frac{f}{f_0} \right)^5 \\
 & \left. \left. + 2681.42 \left(\frac{f}{f_0} \right)^6 \right\} / \left\{ 1 + 13.58 \left(\frac{f}{f_0} \right)^1 - 36.46 \left(\frac{f}{f_0} \right)^2 \right. \right. \\
 & \left. \left. + 18.56 \left(\frac{f}{f_0} \right)^3 + 27.43 \left(\frac{f}{f_0} \right)^4 \right\} \right], \quad (5.22)
 \end{aligned}$$

where $f_0 = 200$ Hz, $f_s = 10$ Hz, and $S_0 = 1.60 \times 10^{-51} \text{ Hz}^{-1}$.

In above equations f_0 , is a scaling frequency chosen to be the frequency at which the noise amplitude is minimum or where the sensitivity is maximum. See Fig. [5.1].

In Fig. [5.1] we plot the noise amplitude for Initial-LIGO, Virgo, Advanced-LIGO and EGO. The ground-based detectors are sensitive in the frequency range 10-1000 Hz. For all the detectors the maximum sensitivity is in the frequency range 100-500 Hz.

5.3.2 Signal to noise ratio

Following the discussion in Sec. 1.9, if $S_h(f)$ is the one-sided noise spectral density of a detector, the inner product between two signals $h_a(t)$ and $h_b(t)$ is defined by

$$(h_a|h_b) \equiv 2 \int_0^\infty \frac{\tilde{h}_a^* \tilde{h}_b + \tilde{h}_b^* \tilde{h}_a}{S_h(f)} df, \quad (5.23)$$

where $\tilde{h}_a(f)$ and $\tilde{h}_b(f)$ are the Fourier transforms of the respective gravitational waveforms $h_a(t)$ and $h_b(t)$. The signal-to-noise ratio (SNR) for a given h is then

$$\rho[h] \equiv (h|h)^{1/2}. \quad (5.24)$$

In the stationary phase approximation (SPA), the Fourier transform of the restricted waveform can be shown to be [205]:

$$\tilde{h}(f) = \bar{\mathcal{A}} f^{-7/6} e^{i\psi(f)}, \quad (5.25a)$$

$$\text{where, } \bar{\mathcal{A}} = \frac{1}{\sqrt{30}\pi^{2/3}} \frac{\mathcal{M}^{5/6}}{D_L}, \quad (5.25b)$$

where $\bar{\mathcal{A}}$ is the average of \mathcal{A} over all orientation.

With the restricted post-Newtonian form for \tilde{h} in Eq. (5.25), with help of Eq. (5.24) we can express the SNR ρ in the form

$$\rho = 2 \bar{\mathcal{A}} \sqrt{\int_{f_{\text{in}}}^{f_{\text{end}}} \frac{f^{-7/3}}{S_h(f)} df}, \quad (5.26)$$

In Fig. [5.2] we plot the variation in the SNR ρ at a luminosity distance $D_L = 200$ Mpc as a function of the total binary mass using Eq. (5.26) for EGO, Advanced-LIGO, Initial-LIGO and Virgo detectors respectively. We choose 200 Mpc for these calculations since it is expected that the advanced interferometers will detect a few NS-NS events per year at this distance and BH-BH binaries lead to large enough SNR's to implement these tests [28].

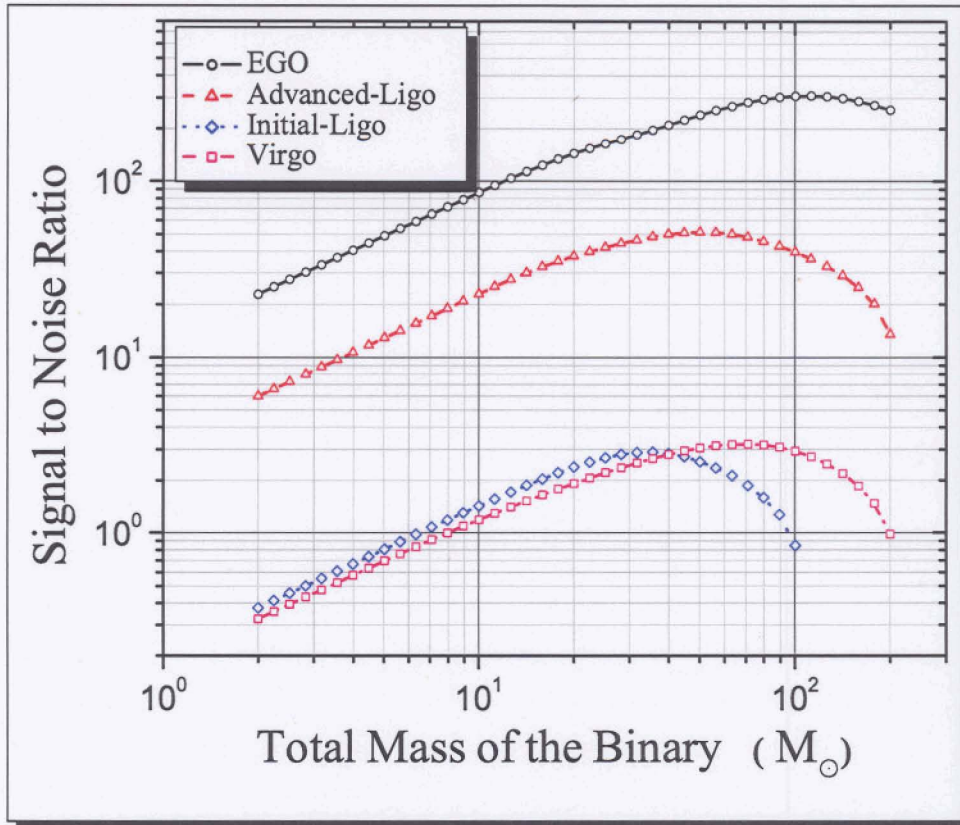


Figure 5.2: SNR of ground-based detectors, current and future, for equal mass binaries as a function of the total mass of the binary M for the luminosity distance $D_L = 200$ Mpc. The typical SNR for neutron-neutron star (NS-NS) binaries at 200 Mpc varies from 0.2 for Initial-LIGO to 30 for EGO. For Virgo and Advanced-LIGO the corresponding values are 0.3 and 8 respectively. A black hole binary of total mass $20M_\odot$ leads to a SNR of 2, 2.25, 25 and 135 in Initial LIGO, VIRGO, Advanced-LIGO and EGO respectively. Initial-LIGO achieves a maximum SNR = 3 corresponding to a total mass of about $\sim 35 M_\odot$. The corresponding numbers for Virgo, Advanced-LIGO and EGO are ~ 3 and $\sim 70 M_\odot$; ~ 50 and $\sim 50 M_\odot$; and ~ 300 and $\sim 200 M_\odot$ respectively.

From the figure it is clear that the typical SNR for neutron-neutron star (NS-NS) binaries at 200 Mpc varies from 0.2 for Initial-LIGO to 30 for EGO. For Virgo and Advanced-LIGO the corresponding values are 0.3 and 8 respectively. For BBH with total mass $40M_{\odot}$ the corresponding values are 3, 3, 50, 100 for Initial-LIGO, Virgo, Advanced-LIGO and EGO respectively. Not only is each detector the most sensitive at different values of the frequency but also the maximum SNR attained by them differs. For Initial-LIGO it is ~ 3 at total mass $\sim 35 M_{\odot}$, whereas, for Virgo it is ~ 3 at total mass $\sim 70 M_{\odot}$. For Advanced-LIGO on the other hand, it is ~ 50 at total mass $\sim 50 M_{\odot}$ while for EGO, it is ~ 300 at total mass $\sim 200 M_{\odot}$. Thus the technological advances are expected to improve the SNR for EGO by about 100 times that of Virgo and for Advanced LIGO by about 20 times that of Initial-LIGO.

5.4 Testing general relativity with gravitational wave observations

Our proposal to test the PN theory is the following. Let us suppose we have a GW event with a high signal-to-noise ratio (SNR), say more than 1,000. Once an event is identified we suggest to fit the data to a signal wherein *each* term in the PN expansion is treated as an independent parameter. More precisely, instead of fitting the detector output with a signal that depends on *only the two* mass parameters, we could fit it with the same signal but by treating *all* the ψ_k 's (cf. Eq. (5.11)) as independent. For example, if we want to test the PN theory to order v^4 then we should use a four-dimensional grid of templates consisting of $\{\psi_0, \psi_2, \psi_3, \psi_4\}$ rather than the two-dimensional one that is used in the detection problem. This higher-dimensional fitting of the data with our model would measure each of the PN coefficients independently of the others. In Einstein's theory, for the case of non-spinning binaries, each of the ψ_k 's has a specific relationship to the masses, $\psi_k = \psi_k(m_1, m_2)$, whereas in a different theory of gravity (for example, a theory in which the graviton has non-zero mass) the relationship will be different and might involve new parameters. Thus, the measured ψ_k 's could be interpreted, in principle, in the context of different theories of gravitation.

In the case of general relativity we know that the ψ_k 's are given in terms of the masses by Eqs. (5.11), (5.14) and (5.17). If general relativity (or, more precisely, the PN theory that approximates general relativity) correctly describes the dynamics of the system then the parameters must be consistent with each other within their respective error bars. One way to check the consistency would be to invert the relationships between the ψ_k 's and the masses to obtain $m_2 = m_2^k(m_1, \psi_k)$, and plot m_2 as a function of m_1 for various ψ_k 's, and see if they all intersect at a common point. If they do, then the theory is correct to within the measurement errors, if not, the theory is in trouble. In addition to the PN theory we

could also test other approximants, such as the P-approximant [39] or the effective one-body approximation [24, 44] that have been proposed as alternatives to the orbital dynamics of binary inspirals as also numerical relativity predictions.

Although these tests are in principle possible, an important question is whether the various PN coefficients can really be measured accurately enough for the test to be meaningful. We already know that a simpler test proposed in Ref. [167], in the context of ground-based detectors, requires events with SNRs in excess of 25. The generalized tests proposed in this chapter would require much stronger signals, SNRs of 100 to test lower-order terms and in excess of 1,000 to test all terms currently known. Initial ground-based interferometers are unlikely to observe events with such large SNRs. As we shall show, while some of these tests might be possible with advanced detectors, a supermassive BBH merger in LISA is our best bet.

To test an approximation it should be possible to measure the various PN coefficients with a good accuracy. We shall require that the relative error in the measurement of a parameter be less than 100%, i.e. $\Delta\psi_k/\psi_k \leq 1$, where $\Delta\psi_k$ is the error in the estimation of the parameter ψ_k , in order that its presence is tested with confidence. A little thought will also reveal that in order to measure more and more higher order PN coefficients independently will require higher SNR's. In the Appendix we summarise the effect on the errors in the lower order coefficients, caused by the increased dimensionality of the parameter space, due to the inclusion of higher order PN coefficients as independent parameters. As expected, covariances between the increasing number of PN parameters systematically worsen the determination of the PN coefficients.

For the binary system in question define a parameter vector $\boldsymbol{\theta} \equiv \{t_c, \Phi_c, \psi_k\}$ for the cases when the log terms are treated as constant or expanded. The parameter vector $\boldsymbol{\theta} \equiv \{t_c, \Phi_c, \psi_k, \psi_{kl}\}$ is chosen in the case when the log terms are treated as independent. We then have

$$\begin{aligned} \Gamma_{ab} &= 4\mathcal{A}^2 \int_{f_s}^{f_{\text{iso}}} f_{ab} f^{-7/3} \frac{df}{S_h(f)}, \\ f_{ab} &\equiv \frac{\partial\Psi(f; \boldsymbol{\theta})}{\partial\theta_a} \frac{\partial\Psi(f; \boldsymbol{\theta})}{\partial\theta_b}. \end{aligned} \quad (5.27)$$

Note that we have now introduced specific values for the limits in the integration: f_s is simply the lower frequency cutoff chosen such that the loss in the SNR due to this choice is negligible compared to the choice $f_s = 0$. f_{iso} is the frequency of the radiation at the last stable orbit of the system which we assume to be the value given in the test mass approximation, namely $f_{\text{iso}} = 1/(6^{3/2}\pi M)$. Using the Fourier domain waveforms given in Eqs. (5.10), (5.13) and (5.16), it is straightforward to compute f_{ab} which is $\boldsymbol{\theta} \times \boldsymbol{\theta}$ matrix in both the log-constant

and log-expanded cases:

$$\begin{bmatrix} 4\pi^2 x^6 & 2\pi x^3 & 2\pi x^{-2} & 2\pi & 2\pi x & 2\pi x^2 & 2\pi x^4 & 2\pi x^5 \\ 2\pi x^3 & 1 & x^{-5} & x^{-3} & x^{-2} & x^{-1} & x & x^2 \\ 2\pi x^{-2} & x^{-5} & x^{-10} & x^{-8} & x^{-7} & x^{-6} & x^{-4} & x^{-3} \\ 2\pi & x^{-3} & x^{-8} & x^{-6} & x^{-5} & x^{-4} & x^{-2} & x^{-1} \\ 2\pi x & x^{-2} & x^{-7} & x^{-5} & x^{-4} & x^{-3} & x^{-1} & 1 \\ 2\pi x^2 & x^{-1} & x^{-6} & x^{-4} & x^{-3} & x^{-2} & 1 & x \\ 2\pi x^4 & x & x^{-4} & x^{-2} & x^{-1} & 1 & x^2 & x^3 \\ 2\pi x^5 & x^2 & x^{-3} & x^{-1} & 1 & x & x^3 & x^4 \end{bmatrix}. \quad (5.28)$$

In the case where the log terms are parametrised by independent parameters, f_{ab} is a 10 x 10 matrix whose first five columns are given by

$$\begin{bmatrix} 4\pi^2 x^6 & 2\pi x^3 & 2\pi x^{-2} & 2\pi & 2\pi x \\ 2\pi x^3 & 1 & x^{-5} & x^{-3} & x^{-2} \\ 2\pi x^{-2} & x^{-5} & x^{-10} & x^{-8} & x^{-7} \\ 2\pi & x^{-3} & x^{-8} & x^{-6} & x^{-5} \\ 2\pi x & x^{-2} & x^{-7} & x^{-5} & x^{-4} \\ 2\pi x^2 & x^{-1} & x^{-6} & x^{-4} & x^{-3} \\ 6\pi x^3 \ln(x) & 3 \ln(x) & 3x^{-5} \ln(x) & 3x^{-3} \ln(x) & 3x^{-2} \ln(x) \\ 2\pi x^4 & x & x^{-4} & x^{-2} & x^{-1} \\ 6\pi x^4 \ln(x) & 3x \ln(x) & 3x^{-4} \ln(x) & 3x^{-2} \ln(x) & 3x^{-1} \ln(x) \\ 2\pi x^5 & x^2 & x^{-3} & x^{-1} & 1 \end{bmatrix},$$

and whose last five columns read

$$\begin{bmatrix} 2\pi x^2 & 6\pi x^3 \ln(x) & 2\pi x^4 & 6\pi x^4 \ln(x) & 2\pi x^5 \\ x^{-1} & 3 \ln(x) & x & 3x \ln(x) & x^2 \\ x^{-6} & 3x^{-5} \ln(x) & x^{-4} & 3x^{-4} \ln(x) & x^{-3} \\ x^{-4} & 3x^{-3} \ln(x) & x^{-2} & 3x^{-2} \ln(x) & x^{-1} \\ x^{-3} & 3x^{-2} \ln(x) & x^{-1} & 3x^{-1} \ln(x) & 1 \\ x^{-2} & 3x^{-1} \ln(x) & 1 & 3 \ln(x) & x \\ 3x^{-1} \ln(x) & 9 \ln(x)^2 & 3x \ln(x) & 9x \ln(x)^2 & 3x^2 \ln(x) \\ 1 & 3x \ln(x) & x^2 & 3x^2 \ln(x) & x^3 \\ 3 \ln(x) & 9x \ln(x)^2 & 3x^2 \ln(x) & 9x^2 \ln(x)^2 & 3x^3 \ln(x) \\ x & 3x^2 \ln(x) & x^3 & 3x^3 \ln(x) & x^4 \end{bmatrix}. \quad (5.29)$$

In the above $x = f^{1/3}$. [Beware of the change in notation for x different from the one normally used in the generation context (See Chapters 2 and 3) where it denotes the gauge-invariant parameter $x = (GmnK/c^3)^{2/3}$.]

We see that the information matrix will involve moments of the noise spectrum of the form $\int_0^\infty f^{-j/3} \frac{df}{S_h(f)}$, where j runs from 1 to 17. The elements of the information matrix, therefore, take on values in a very large range leading to a highly ill-conditioned **matrix**. Extreme caution should be exercised in computing the moments, else it is easy to end up with values in the covariance matrix that are negative, and even imaginary, while we know that the covariance matrix should be real.

5.5 Results for ground-based detectors

In this section we summarise the results following the procedure described in the previous section. We proceed systematically starting from the presently operating ground-based detectors like initial-LIGO and Virgo and moving on to the next generation detectors, Advanced-LIGO and the third generation one like EGO. An examination of these results then makes obvious the need and advantages of going to a space-based detector like LISA, which we analyse later. In each of the cases we have also examined the differences arising from different strategies to treat the log terms in the phasing formula.

In view of the structure of the noise functions of the various detectors mentioned in Sec. 5.3, the integrals in Eq.(5.27) can only be evaluated using numerical methods. We use three different methods to check our evaluations:

- 1) Gauss program using C++ from Numerical Methods [206],
- 2) NIntegrate Package in Mathematica version 5.2, and
- 3) ListIntegrate Package in Mathematica version 5.2.

We used these three methods and varied the number of integration points to check our results for the Fisher information matrix Γ_{ab} . In this regard, we find that irrespective of the three different ways in which the log terms are treated (constant, Taylor expanded or characterized by new independent parameters) the difference in the values of Γ_{ab} coming from the three numerical methods is very small and within the limit of numerical errors. The values of Γ_{ab} do *not* depend on the number of integration points in the range 10^3 to 10^6 . We can thus be confident of our numerical evaluation of the integrals in the definition of the Γ_{ab} .

However, our problem does not end here. We next need to calculate the matrix inverse of Γ_{ab} to obtain Σ_{ab} . In this calculation more serious numerical problems arise because of the ill-conditioned nature of the matrix Γ_{ab} especially in the higher mass range. The numerics in this case seem to be very sensitive to the precision used and a careful analysis showed that the problem is alleviated to a large extent by using 'infinite precision'. More explicitly, the

use of a rational number representation of the matrix elements in our **Mathematica** programs seems to circumvent the problem of a badly computed matrix inverse. With this prescription the inverse is numerically well determined ($\Gamma \cdot \Sigma = \mathbf{I}$!) as long as the determinant of Γ_{ab} is well within the machine precision. For high values of mass the determinant is either too large or too small and in these cases there are large differences in the values of Σ_{ab} [including even (the obviously incorrect) imaginary values] between the different methods. In particular, note that for all the detectors and for the case where the log terms are treated as independent parameters the curves are not smooth and the data points are fewer. See Figures [5.3] and [5.4]. This could be due to the fact that when the dimensionality of the parameter space increases, the covariance matrix is highly ill-conditioned leading to an unreliable inverse. For many values of the binary mass the unreliable numerical situation leads to unphysical imaginary values resulting in fewer reliable points and a consequent more jagged curve. For a lower range of masses (and other ways of dealing with logs), the curves are smooth and this leads us to believe in their reliability. More careful studies are needed to deal with these delicate numerical issues and ascertain the reliability of the results in the problematic mass ranges. We hope to return to this in the future.

Let us begin with a study of the current generation detectors **Initial- LIGO** and **Virgo**. Fig. [5.3] plots the relative errors in ψ_k 's at $D_L = 200$ Mpc in a six panel format. The top panels corresponds to **Virgo** and the bottom panels to **Initial LIGO**. The first column on the other hand corresponds to the case where the log terms are treated as constants, the second column where the log terms are Taylor-expanded and retained up to **3.5PN** and finally the third column where the log terms are treated as independent terms and parameterized by new additional parameters. From the first row for the **Virgo** detector we see that we can only test the lowest order parameter ψ_0 and that too for a very small range of binary masses. Even so, this is only possible for the first two ways of dealing with logarithms, (either in the constant log or in the expanded log case). For **Initial LIGO** *none* of the ψ_k 's can be tested.

We next move on to the next generation detectors, **Advanced LIGO** and **EGO**. Fig. [5.4] summarizes similarly the situation for these two detectors with **Advanced LIGO** in the top panels and **EGO** in the bottom panels. From the figures one can see that for **Advanced LIGO** once again one can only test ψ_0 . However it can be tested for a larger range of binary masses in the log-constant and log-expanded cases and even for the log-independent case though for a smaller range of masses. With **EGO** the situation is the best among the ground-based detectors. Not only ψ_0 but also ψ_2 can be tested, both in the log-constant and log-expanded cases. However when the log terms are independently parametrised *only* ψ_0 can be tested.

From the discussion of the results above for ground-based detectors, both present and future third generation, it is clear that one can only test PN theory to order 1PN at most, and as expected with a binary black hole system. Testing the higher order PN terms would

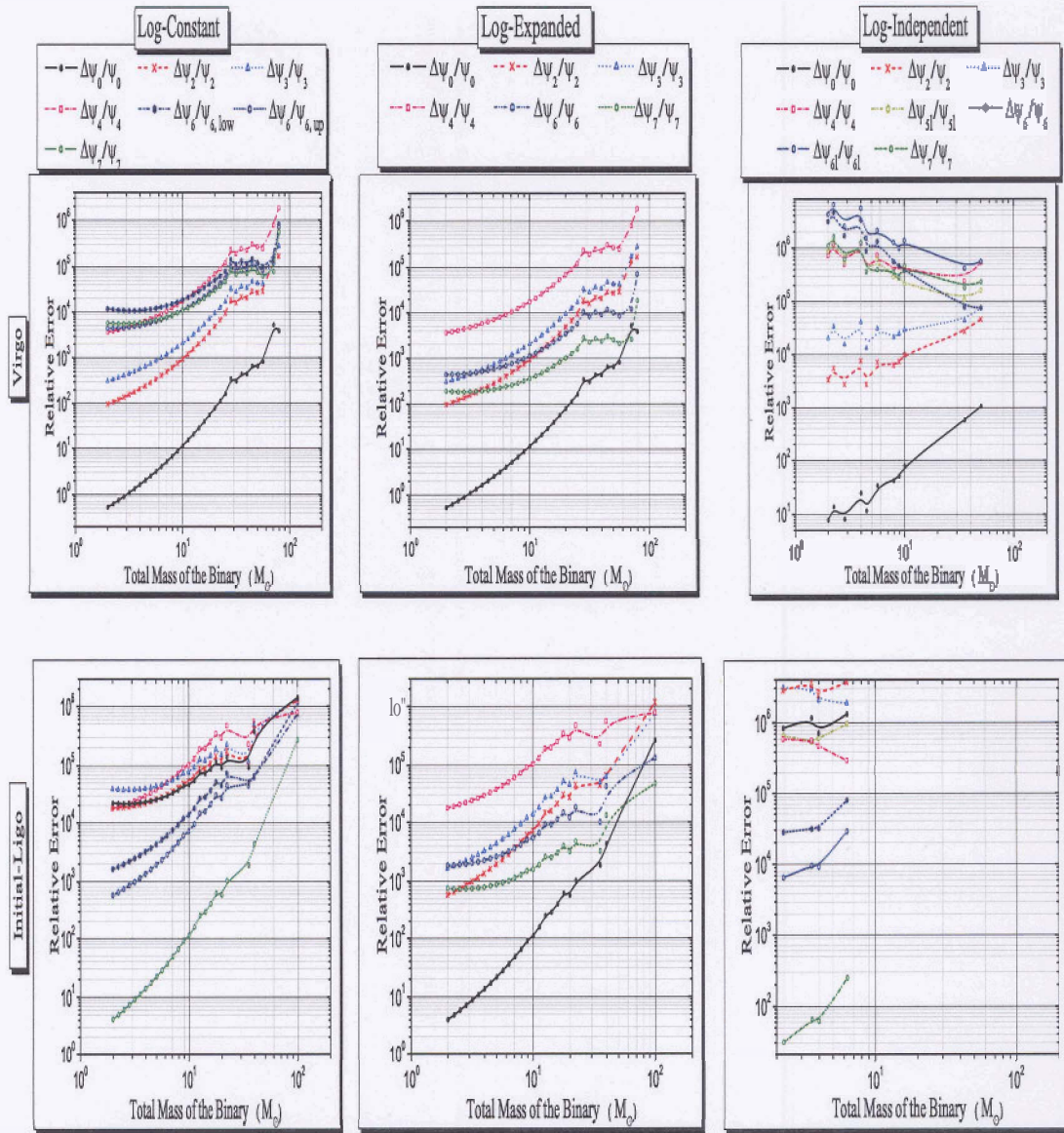


Figure 5.3: Relative errors in ψ_k as a function of the total mass of the binary M for Virgo (Top Panels) and Initial-LIGO (Bottom Panels) and three different ways of dealing with the log terms: The first column where the log terms are treated as constants, the second column where the log terms are Taylor expanded about v_{iso} and retained to 3.5PN and the third column where the log terms are parameterized by independent parameters. The source is at luminosity distance of $D_L = 200$ Mpc. For Virgo (both when the log terms are treated as constants or are expanded), only ψ_0 can be tested and that too only in a small range of masses ($2-3M_\odot$). If the log terms are parameterized by independent parameters none of the ψ_k 's can be tested at the luminosity distance of $D_L = 200$ Mpc. For Initial-LIGO, in all the three cases, none of the ψ_k 's can be tested at $D_L = 200$ Mpc.

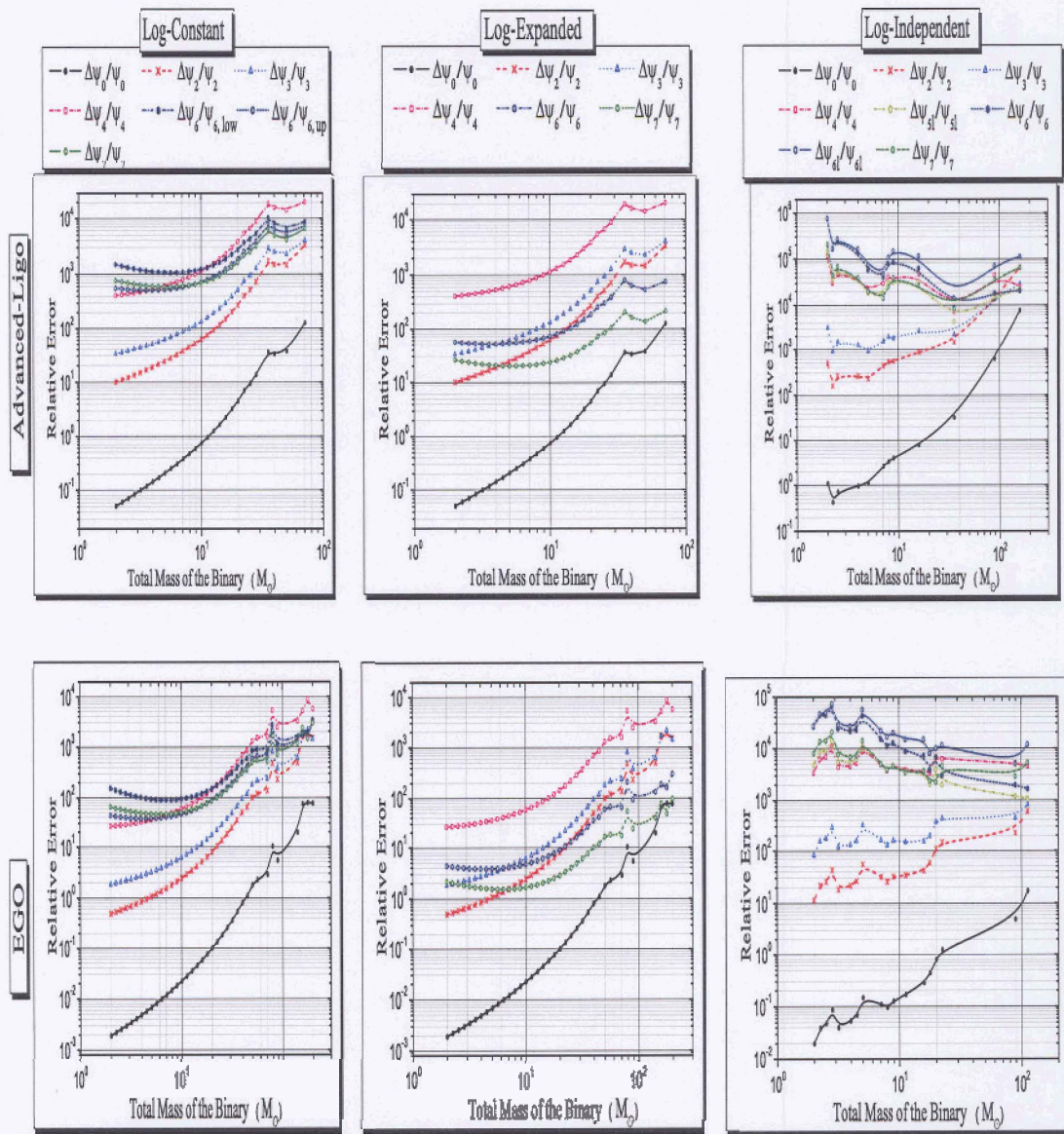


Figure 5.4: Relative errors in ψ_k as a function of the total mass of the binary M for Advanced-LIGO (Top Panels) and EGO (Bottom Panels) and three different ways of dealing with the log terms: The first column where the log terms are treated as constants, the second column where the log terms are Taylor expanded about v_{iso} and retained to 3.5PN and the third column where the log terms are parameterized by independent parameters. The source is at luminosity distance of $D_L = 200$ Mpc. For Advanced-LIGO (and in all three ways of treating the log terms), only ψ_0 can be tested. The range of masses is bigger and corresponds to $(2 \sim 10 M_\odot)$. For EGO (in all the three cases) ψ_0 can be tested for a wide range of binary masses. Further, ψ_2 can be tested (if the log terms are treated as constants or Taylor expanded) in the range $(2 \sim 4 M_\odot)$.

require larger SNRs and these are expected in space-based GW detectors like LISA. In the next section, we explore this possibility in more detail.

5.6 Space-based detector-LISA

The Laser Interferometric Space Antenna (LISA) will observe supermassive black hole binary mergers with amplitude signal-to-noise ratio of several thousands. We investigate the extent to which such observations afford high-precision tests of Einstein's gravity. We show that LISA provides a unique opportunity to probe the non-linear structure of post-Newtonian theory both in the context of general relativity and its alternatives.

There are some major differences between the ground-based detectors discussed in the previous section and space detector like LISA. The important difference is that LISA will be sensitive to gravitational waves in a much lower frequency band: 10^{-4} - 10^{-1} Hz, a frequency range not accessible to the ground-based detectors due to seismic and more importantly gravity gradient noise. Another important difference between LISA and the ground-based interferometers relates to how they identify the angular position of the source in the sky. LISA is not a pointed instrument; it is an all-sky monitor with a **quadrupolar** beam pattern. The ground-based detectors share this characteristic, but because there will be at least three ground-based detectors, and because they will be sensitive to gravitational radiation whose wavelength is much shorter than the distance between detectors, they will be able to determine the source position to within $\sim 1^\circ$ by a standard time-of-flight method [20]. This method is not available to LISA. Only one space-based detector is currently planned. Moreover the gravitational wavelength at the heart of the LISA band ($\sim 10^3$ Hz) is of order 1 AU, so a second detector would have to be placed at least several AU away from the Earth for time-of-flight measurements to give useful constraints on source positions [207]. The argument presented here is not the full story. LISA measures the direction to its sources in the same way as a *single* ground-based interferometer measures direction to a GW source, viz by demodulating the doppler modulation on the waveform due to the motion of LISA relative to the source.

The frequency band, 10^{-4} - 10^{-1} Hz, contains many known gravitational wave sources that LISA is able to see. These guaranteed sources comprise a wide variety of short-period binary star systems, both galactic and extragalactic, including close white dwarf binaries, interacting white dwarf binaries, unevolved binaries, W Ursae Majoris (W UMa)⁴ binaries and neutron star binaries.

Indeed, our galaxy probably contains so many short-period, stellar-mass binaries that LISA will be unable to resolve them individually, and the resulting confusion noise will ac-

⁴W UMa is a variable star in the constellation Ursa Major.

tually dominate over instrumental noise at frequencies $\lesssim 10^{-3}$ Hz, as the principal obstruction to finding other sources of GWs in the data-stream. In addition to stellar-mass binaries, other possible LISA sources include: a stochastic GW background generated in the early universe, the inspiral of compact, stellar-mass objects into supermassive black holes (SMBHs) and the merger of two SMBHs . The detection of any one of these would clearly be of immense interest. The events involving supermassive black holes must surely occur in the universe, but the event rates are highly uncertain [207].

5.6.1 Sensitivity curve of LISA

The power-spectral-density of LISA is more complex and includes both instrumental and astrophysical contributions. The details are beyond the scope of the present study and treated in e.g. [207, 208, 209, 196]. We only list the expressions we require. The total noise curve of LISA is given by [196]

$$S_h(f) = \min \left\{ S_h^{\text{NSA}}(f) / \exp(-\kappa T_{\text{mission}}^{-1} dN/df), S_h^{\text{NSA}}(f) + S_h^{\text{gal}}(f) \right\} + S_h^{\text{ex-gal}}(f). \quad (5.30)$$

In the above $S_h^{\text{NSA}}(f)$ denotes the non-sky-averaged noise spectral density of LISA and is given by

$$S_h^{\text{NSA}}(f) = \left[9.18 \times 10^{-52} \left(\frac{f}{f_0} \right)^{-4} + 1.59 \times 10^{-41} + 9.18 \times 10^{-38} \left(\frac{f}{f_0} \right)^2 \right] \text{Hz}^{-1}. \quad (5.31)$$

$S_h^{\text{gal}}(f)$ is the galactic estimated white-dwarf confusion noise which is approximated as

$$S_h^{\text{gal}}(f) = 2.1 \times 10^{-45} \left(\frac{f}{f_0} \right)^{-7/3} \text{Hz}^{-1}. \quad (5.32)$$

Finally, $S_h^{\text{ex-gal}}(f)$ is the contribution from extra-galactic white dwarfs and given by

$$S_h^{\text{ex-gal}}(f) = 4.2 \times 10^{-47} \left(\frac{f}{f_0} \right)^{-7/3} \text{Hz}^{-1}. \quad (5.33)$$

In the expression above $f_0 = 1$ Hz and dN/df the number density of galactic white-dwarf binaries per unit gravitational-wave frequency, represented as

$$\frac{dN}{df} = 2 \times 10^{-3} \text{Hz}^{-1} \left(\frac{1 \text{Hz}}{f} \right)^{11/3}. \quad (5.34)$$

In our calculations we always assume that the duration of the LISA mission $T_{\text{mission}} = 1$ yr and $\kappa \simeq 4.5$ [196].

5.7 Antenna pattern function for LISA detector

The signal measured by LISA, $h(t)$, can be written as:

$$h(t) = \frac{\sqrt{3}}{2} \frac{2m_1 m_2}{r(t) D_L} \tilde{A}(t) \cos \left(\int_0^t f(t') dt' + \varphi_p(t) + \varphi_D(t) \right), \quad (5.35)$$

where $r(t)$ is the relative distance between the two compact bodies, $\varphi_p(t)$ is the waveform polarization phase [see Eq. (5.39a)] and $\varphi_D(t)$ the Doppler phase [see Eq. (5.39b)]. $\tilde{A}(t)$ is defined by

$$\tilde{A}(t) = \sqrt{[1 + (\hat{\mathbf{L}} \cdot \mathbf{n})^2]^2 F^{+2} + 4(\hat{\mathbf{L}} \cdot \mathbf{n})^2 F^{\times 2}}. \quad (5.36)$$

where $\hat{\mathbf{L}}$ is the orbital angular momentum unit vector of the source, and \mathbf{n} is a unit vector in the direction of the source on the sky. The quantities $F^{+, \times}$ are the pattern functions, defined by

$$\begin{aligned} F^+(\theta_S, \phi_S, \psi_S) &= \frac{1}{2}(1 + \cos^2 \theta_S) \cos 2\phi_S \cos 2\psi_S \\ &\quad - \cos \theta_S \sin 2\phi_S \sin 2\psi_S, \\ F^\times(\theta_S, \phi_S, \psi_S) &= \frac{1}{2}(1 + \cos^2 \theta_S) \cos 2\phi_S \sin 2\psi_S \\ &\quad + \cos \theta_S \sin 2\phi_S \cos 2\psi_S. \end{aligned} \quad (5.37)$$

In the above equations we have denoted by (θ_S, ϕ_S) the source location and by ψ_S the polarization angle defined as

$$\tan \psi_S(t) = \frac{\hat{\mathbf{L}} \cdot \mathbf{z} - (\hat{\mathbf{L}} \cdot \mathbf{n})(\mathbf{z} \cdot \mathbf{n})}{\mathbf{n} \cdot (\hat{\mathbf{L}} \times \mathbf{z})}, \quad (5.38)$$

with $\hat{\mathbf{L}}$, \mathbf{z} and $-\mathbf{n}$ being the unit vectors along the orbital angular momentum, the unit normal to LISA's plane and the GW direction of propagation, respectively.

The waveform polarization and Doppler phases that will enter the GW signal (see Eq. (5.42) later) are

$$\varphi_p(t) = \tan^{-1} \left[\frac{2(f, \mathbf{n}) F^\times(t)}{(1 + (\hat{\mathbf{L}} \cdot \mathbf{n})^2) F^+(t)} \right], \quad (5.39a)$$

$$\varphi_D(t) = \frac{2\pi f}{c} R \sin \bar{\theta}_S \cos(\bar{\phi}(t) - \bar{\phi}_S), \quad (5.39b)$$

with $R = 1 \text{ AU}$ and $\bar{\phi}(t) = \bar{\phi}_0 + 2\pi t/T$. Here $T = 1 \text{ year}$ is the orbital period of LISA, and $\bar{\phi}_0$ is a constant that specifies the detector's location at time $t = 0$. In this chapter we always assume that there is no precession, so \hat{L}^a points in a fixed direction $(\bar{\theta}_L, \bar{\phi}_L)$. The angles $\bar{\theta}_S, \bar{\phi}_S, \bar{\theta}_L, \bar{\phi}_L$ describe the source location and orbital angular momentum direction in the reference frame attached to the solar system barycenter.

The relations between the angles $(\theta_S, \phi_S, \psi_S)$ evaluated with respect to the rotating detector-based coordinate system and the angles $(\bar{\theta}_S, \bar{\phi}_S, \bar{\theta}_L, \bar{\phi}_L)$ evaluated with respect to the fixed solar-system-based coordinate system are given by [207]:

$$\cos \theta_S(t) = \frac{1}{2} \cos \bar{\theta}_S - \frac{\sqrt{3}}{2} \sin \bar{\theta}_S \cos(\bar{\phi}(t) - \bar{\phi}_S), \quad (5.40a)$$

$$\phi_S(t) = \bar{\alpha}_0 + \frac{2\pi t}{T} + \tan^{-1} \left[\frac{\sqrt{3} \cos \bar{\theta}_S + \sin \bar{\theta}_S \cos(\bar{\phi}(t) - \bar{\phi}_S)}{2 \sin \bar{\theta}_S \sin(\bar{\phi}(t) - \bar{\phi}_S)} \right], \quad (5.40b)$$

where $\bar{\alpha}_0$ is a constant specifying the orientation of the arms at $t = 0$. Following Cutler [207], we choose $\bar{\alpha}_0 = 0$ and $\bar{\phi}_0 = 0$, corresponding to a specific choice of the initial position and orientation of the detector. In addition [207, 196],

$$\mathbf{z} \cdot \mathbf{n} = \cos \theta_S, \quad (5.41a)$$

$$\hat{\mathbf{L}} \cdot \mathbf{z} = \frac{1}{2} \cos \bar{\theta}_L - \frac{\sqrt{3}}{2} \sin \bar{\theta}_L \cos(\bar{\phi}(t) - \bar{\phi}_L), \quad (5.41b)$$

$$\mathbf{L} \cdot \mathbf{n} = \cos \bar{\theta}_L \cos \bar{\theta}_S + \sin \bar{\theta}_L \sin \bar{\theta}_S \cos(\bar{\phi}_L - \bar{\phi}_S), \quad (5.41c)$$

$$\begin{aligned} \mathbf{n} \cdot (\hat{\mathbf{L}} \times \mathbf{z}) &= \frac{1}{2} \sin \bar{\theta}_L \sin \bar{\theta}_S \sin(\bar{\phi}_L - \bar{\phi}_S) \\ &\quad - \frac{\sqrt{3}}{2} \cos \bar{\phi}(t) \left(\cos \bar{\theta}_L \sin \bar{\theta}_S \sin \bar{\phi}_S - \cos \bar{\theta}_S \sin \bar{\theta}_L \sin \bar{\phi}_L \right) \\ &\quad - \frac{\sqrt{3}}{2} \sin \bar{\phi}(t) \left(\cos \bar{\theta}_S \sin \bar{\theta}_L \cos \bar{\phi}_L - \cos \bar{\theta}_L \sin \bar{\theta}_S \cos \bar{\phi}_S \right). \end{aligned} \quad (5.41d)$$

The Fourier transform of the measured signal can be evaluated in the stationary phase approximation, since $\tilde{A}(t)$, $\varphi_p(t)$ and $\varphi_D(t)$ vary on time scales on the order of 1 year (thus much larger than the binary orbital period $\approx 2/f$). The result is

$$\tilde{h}(f) = \frac{\sqrt{3}}{2} \tilde{\mathcal{A}} f^{-7/6} e^{i\Psi(f)} \left\{ \frac{5}{4} \tilde{A}(t(f)) \right\} e^{-i(\varphi_{p,\alpha}(t(f)) + \varphi_D(t(f)))}, \quad (5.42)$$

where $\tilde{\mathcal{A}}$ is defined in Eq. (5.25b), and $t(f)$ is given by

$$t(f) = \frac{1}{2\pi} \frac{d\Psi(f)}{df}. \quad (5.43)$$

To proceed we list below the explicit expression for $t(f)$ we will require in the computation in the different methods of dealing with the log terms.

1. Log-Constant:

$$t(f) = t_c + \frac{1}{2\pi} \sum_k \frac{k-5}{3} \psi_k f^{(k-8)/3}, \quad (5.44)$$

Chapter 5

where ψ_k are given by Eq. (5.10).

2. Log-Expanded:

$$t(f) = t_c + \frac{1}{2\pi} \sum_k \frac{k-5}{3} \psi_k f^{(k-8)/3} \quad (5.45)$$

here ψ_k are given by Eq. (5.13).

3. Independent parameter for log terms:

$$t(f) = t_c + \frac{1}{2\pi} \sum_k \left\{ \frac{k-5}{3} [\psi_k + \psi_{kl} \ln(f)] + \psi_{kl} \right\} f^{(k-8)/3} \quad (5.46)$$

where ψ_k are given by Eq. (5.16).

5.7.1 Signal to noise ratio with orientation pattern

From the general definition of SNR in Eq. (5.24), the non-averaged SNR is given by

$$\rho(\bar{\theta}_S, \bar{\phi}_S, \bar{\theta}_L, \bar{\phi}_L) = \frac{5}{2} \bar{\mathcal{A}} \sqrt{\int_{f_{\text{in}}}^{f_{\text{end}}} \frac{3}{4} \bar{A}^2(t(f); \bar{\theta}_S, \bar{\phi}_S, \bar{\theta}_L, \bar{\phi}_L) \frac{f^{-7/3}}{S_h(f)} df}. \quad (5.47)$$

Following [196] the limits in the integral appearing in the above equation can be chosen. The upper limit of integration is $f_{\text{in}} = \min(f_{\text{ISCO}}, f_{\text{end}})$. Here f_{ISCO} is twice the conventional (Schwarzschild) frequency of the innermost stable circular orbit for a point mass, namely $f_{\text{ISCO}} = (6^{3/2} \pi M)^{-1}$, and $f_{\text{end}} = 1$ Hz is a conventional upper cutoff on the LISA noise curve. The initial frequency f_{in} in the integrals of the Fisher matrix is determined by assuming that we observe the inspiral over a time T_{obs} before the ISCO, and by selecting a cutoff frequency below which the LISA noise curve is not well characterized. Our default cutoff is $f_{\text{low}} = 10^{-5}$ Hz. The initial frequency is then given, in Hz, by the larger of these frequencies,

$$f_{\text{in}} = \max \left\{ f_{\text{low}}, 4.149 \times 10^{-5} \left[\frac{\mathcal{M}}{10^6 M_{\odot}} \right]^{-5/8} \left(\frac{T_{\text{obs}}}{1 \text{ yr}} \right)^{-3/8} \right\}. \quad (5.48)$$

The frequency at a given observation time is calculated using the quadrupole approximation for radiation damping. In our calculations we assume that $T_{\text{obs}} = 1$ yr, consistently with the choice we made for the LISA mission duration T_{obs} in Eq. (5.30).

In the Fig. [5.5] we plot the signal to noise ratio (SNR) for different orientations for the sources at a luminosity distance $D_L = 3$ Gpc starting from the orientation $\{\theta_S, \phi_S, \theta_L, \phi_L\} = \{(13/40)\pi, \pi, (27/40)\pi, 0\}$, which gives a large SNR. The other directions have been arbi-

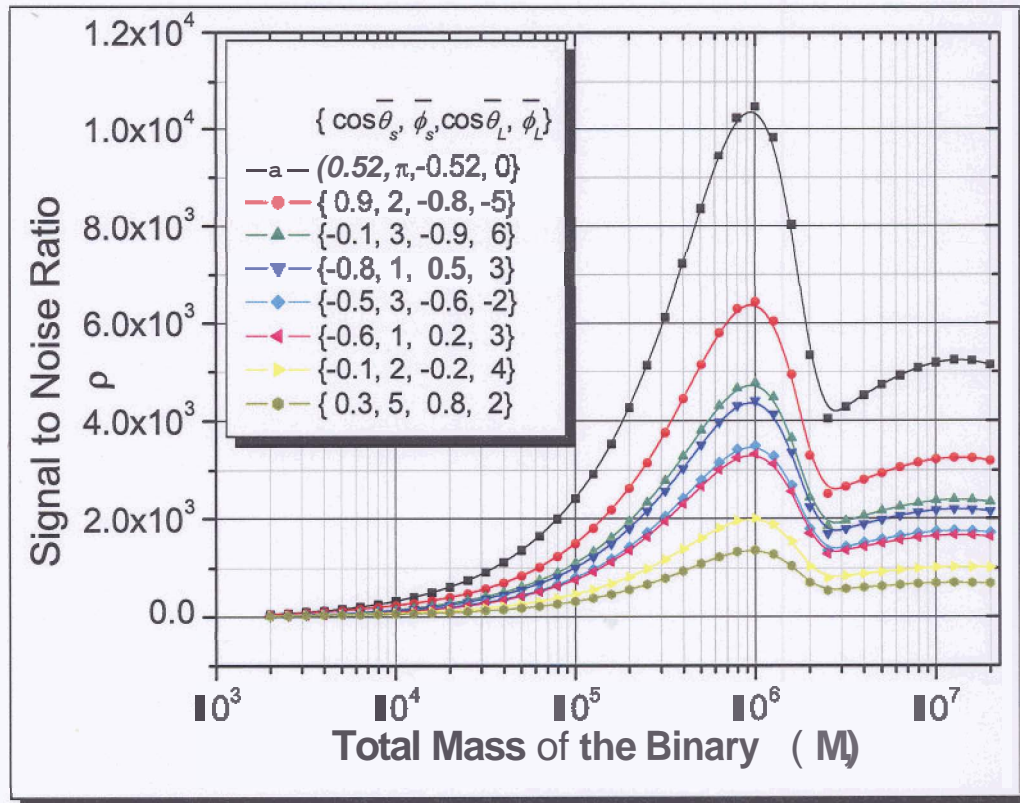


Figure 5.5: Signal to noise ratio ρ for LISA as a function of total mass of the binary (in M_{\odot}) located at a luminosity distance $D_L = 3000$ Mpc. $(\bar{\theta}_S, \bar{\phi}_S, \bar{\theta}_L, \bar{\phi}_L)$ describe the source location and orbital angular momentum direction in the reference frame attached to the solar system barycenter. In our calculations, we use the orientation $(\cos \bar{\theta}_S, \bar{\phi}_S, \cos \bar{\theta}_L, \bar{\phi}_L) = (0.9, 2, -0.8, -5)$ (“optimally oriented”) for which the maximum SNR is $\approx 6.4 \times 10^3$ for a binary mass 10^6 . Even in this limited set of angles there exists an orientation which gives a larger SNR $\approx 1.15 \times 10^4$ at the total binary mass 10^6 .

rarily taken. For all the curves the maximum values of SNR appear at total mass $10^6 M_\odot$. The dips which occur at $2 \times 10^6 M_\odot$ are due to the white-dwarf confusion noise.

5.8 Pattern averaged waveform and its SNR

Taking the average of the waveform for one LISA detector over the pattern functions in the stationary phase approximation, the waveform in the Fourier domain is given by

$$\tilde{h}(f) = \frac{\sqrt{3}}{2} \bar{\mathcal{A}} f^{-7/6} e^{i\psi(f)}. \quad (5.49)$$

Recall, that using Eq. (5.24), we can express the SNR ρ in the form

$$\rho = 2 \mathcal{A} \sqrt{\int_{f_{\text{in}}}^{f_{\text{end}}} \frac{3 \mathcal{E}^{-7/3}}{4 S_h(f)} df}, \quad (5.50)$$

The limits in the integral have already been discussed in the previous Sec. 5.7.1.

Fig. [5.6] shows the SNR with averaged orientation waveform pattern and with one particular orientation pattern waveform. The orientation of the source is chosen to be $(\cos \bar{\theta}_S, \bar{\phi}_S, \cos \bar{\theta}_L, \bar{\phi}_L) = (0.9, 2, -0.8, -5)$ an "optimal orientation" in the sense that it leads to a high SNR. The two curves in the log-log scale look almost parallel. The maximum SNR for both curves is more than 4000 and 6000 respectively and they occur at total mass of MBBH of $10^6 M_\odot$.

5.9 Parameter estimation for LISA

In this section we discuss our results for parameter estimation using the LISA noise PSD. The results for the two cases, one where the pattern averaged waveform is used and the other where waveform is used without pattern averaging, are explained. For the case when one ignores the antenna pattern of LISA (which assumes that source lasts for smaller duration in the LISA band that modulations are not significant), the analysis is very much similar to the ground-based detectors.

The calculation is more involved when one incorporates the modulations induced by LISA motion. The dimensionality of the parameter space is increased, as compared to the previous cases, by five. Luminosity distance D_L , and the four angles corresponding to the source's location and orientation in the sky are added to the space of parameters. Thus in this case, when logs are treated as constants, the total dimensionality is 13. It increases to 15 when one treats logs as independent parameters. Another difference in the calculation is the

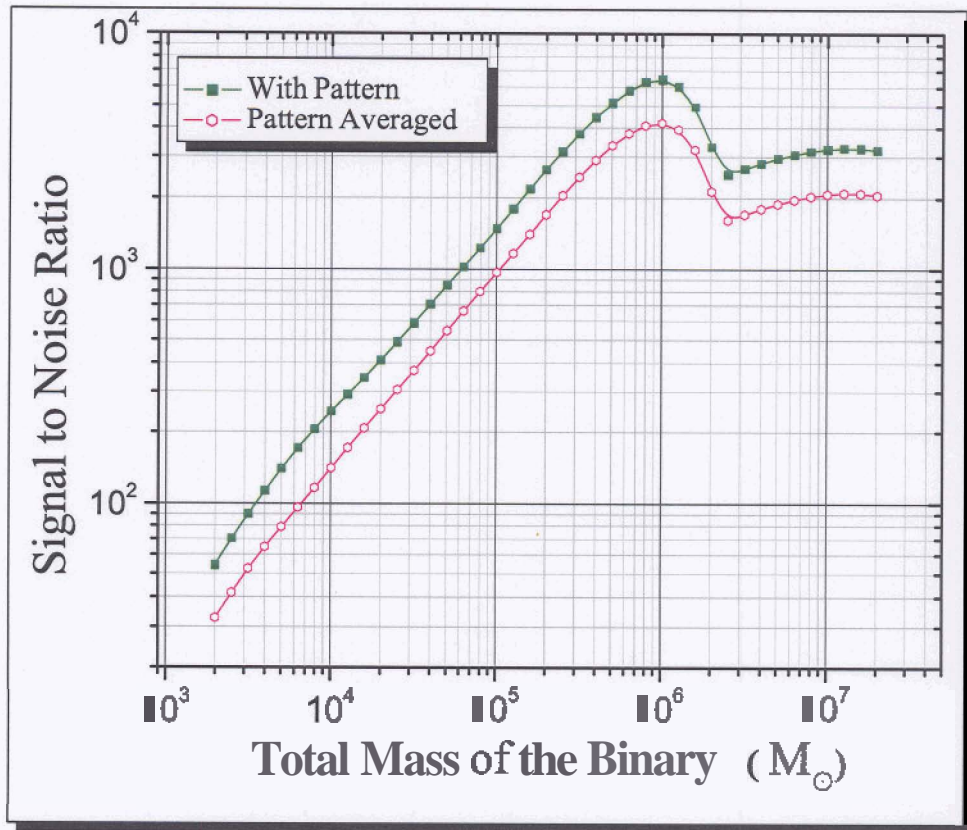


Figure 5.6: Signal to Noise Ratio ρ for LISA as a function of total mass of the binary (in M_{\odot}) located at a luminosity distance $D_L = 3000$ Mpc., for two cases: 1) using orientation pattern waveform where the orientation of the source is chosen to be $(\cos \bar{\theta}_S, \bar{\phi}_S, \cos \bar{\theta}_L, \bar{\phi}_L) = (0.9, 2, -0.8, -5)$, an "optimal orientation". 2) pattern averaged case. The two curves on this scale look parallel. The maximum SNR for both curves is more than 4000 and 6000 respectively and they occur at a binary mass of $10^6 M_{\odot}$. The white-dwarf confusion noise is responsible for the dip in the curves at masses $\sim 2 \times 10^6 M_{\odot}$.

occurrence of $t(f)$ of Eq. (5.43) to account for the amplitude and phase modulations. As is evident from Eq. (5.43), the expression for $t(f)$ has an additional dependence on $\psi_k \mathbf{s}$ which has to be taken into account. Finally, the Fisher matrix is computed incorporating all the above aspects and inverted to obtain the covariance matrix. The results of this exercise are discussed in what follows.

5.9.1 Results for LISA

We shall show in this section that the brightest events that can be expected in the space-based Laser Interferometer Space Antenna (LISA) will test *all* the PN terms computed so far.

We assumed that LISA consists of only one interferometer with sensitivity as in Ref. [207, 208, 196] and the binary consists of two black holes of equal masses in quasi-circular orbit and observed for the last one year before merger.

Fig. [5.7] summarises in a six panel format the relative errors in the various parameters ψ_k as a function of the total mass at a distance of $D_L = 3000$ Mpc. The top panels correspond to the relative error when the pattern orientation waveform is used and the orientation of the sources is chosen to be $(\cos \bar{\theta}_S, \bar{\phi}_S, \cos \bar{\theta}_L, \bar{\phi}_L) = (0.9, 2, -0.8, -5)$ ("optimal orientation"). The bottom panels correspond to the relative error when the averaged waveform pattern is used. As before, the three columns correspond to the three different ways of dealing with log terms. The first column corresponds to the case where the log terms are treated as constants, the second column where the log terms are expanded and retained to be consistent with a 3.5PN accurate waveforms and the third column where the log terms are treated as independent terms and parameterized by two more new parameters. In the first column wherein the log-terms are treated as constants, it is clear that in the mass range $10^5 - 10^6 M_\odot$, fractional errors associated with most of the parameters are less than 1, except for the $\psi_{6,\text{low}} \ni \psi_6(f \rightarrow f_{in})$ which is two times higher. In the second column the case is better: all the relative errors are much small compared to one and for a wide range of masses except for ψ_4 for which the fractional error is less than one only for small range of masses $\sim 2 \times 10^5 M_\odot$. Thus, LISA will provide an unique opportunity to test the PN and related approximations to a high degree of accuracy using the scheme proposed in this chapter. On the scale of the present graph in the first and second columns the visual difference between the top and bottom panels is too small to be critically commented upon. To examine in more detail the difference between the pattern averaged waveform and the waveform including orientation, we plot in Figures [5.8]–[5.10] the two results and in an adjoining panel the associated fractional difference in the case where the log terms treated as constants. From this graph we can conclude that in the mass range $2000 - 2 \times 10^7 M_\odot$ the difference can be as large as 20% for this choice of orientation. However, one must beware that this is not a generic statement and

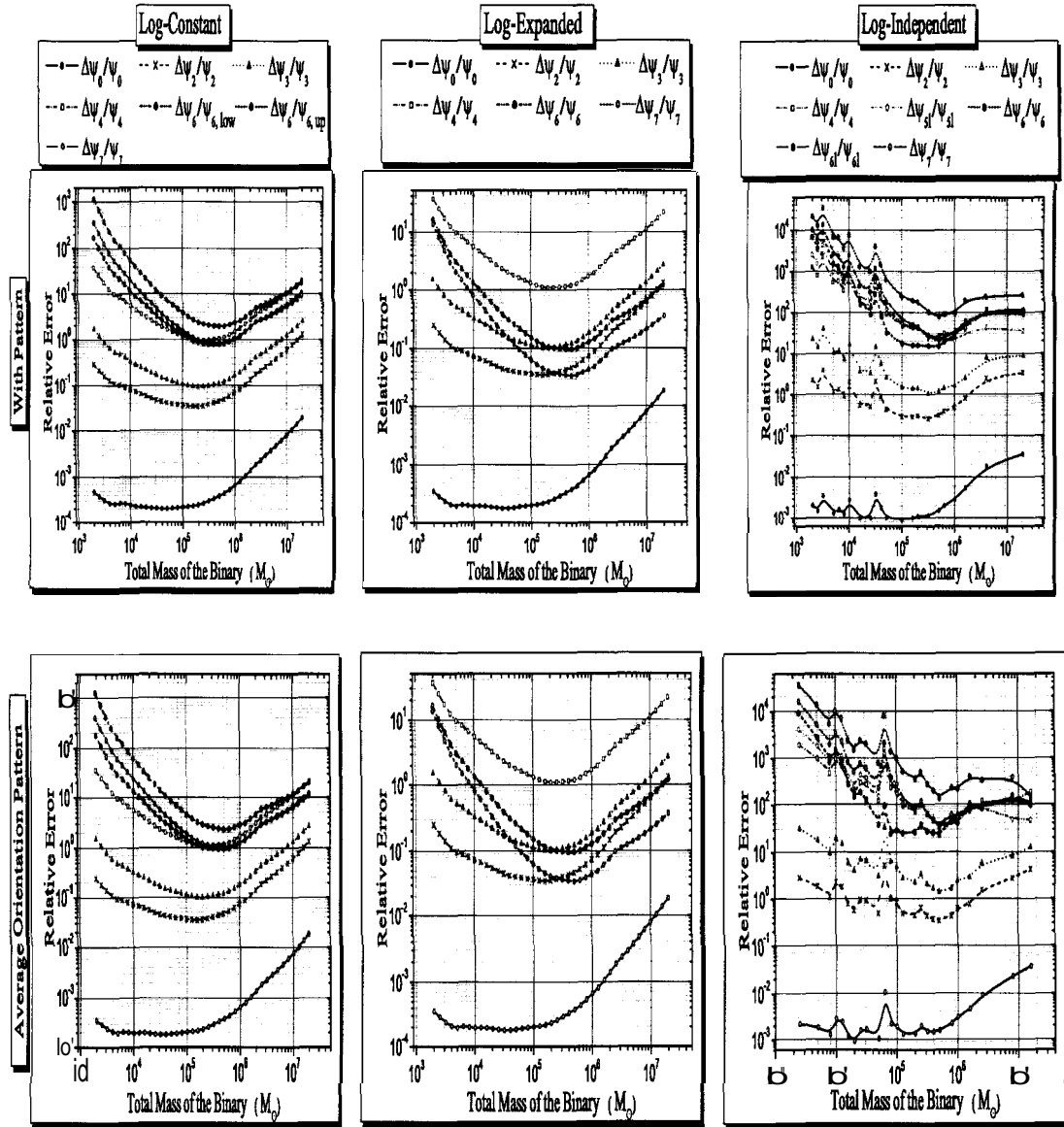


Figure 5.7: Relative errors in ψ_k as a function of the total mass of the binary M for the LISA Detector. The top panels correspond to the case with orientation pattern. The orientation of the source is chosen to be $(\cos \bar{\theta}_S, \bar{\phi}_S, \cos \bar{\theta}_L, \bar{\phi}_L) = (0.9, 2, -0.8, -5)$, an "optimal orientation". The bottom panel corresponds to the case with an average orientation pattern. As before the three columns correspond to the three ways of dealing with logs: log-constant, log-expanded and log-independent respectively. The luminosity distance is $D_L = 3000$ Mpc. In the top panels (when the log terms are treated as constants or Taylor expanded), all the ψ 's, except ψ_{6low} , can be tested in the mass range between $(2-3) \times 10^5$.

Chapter 5

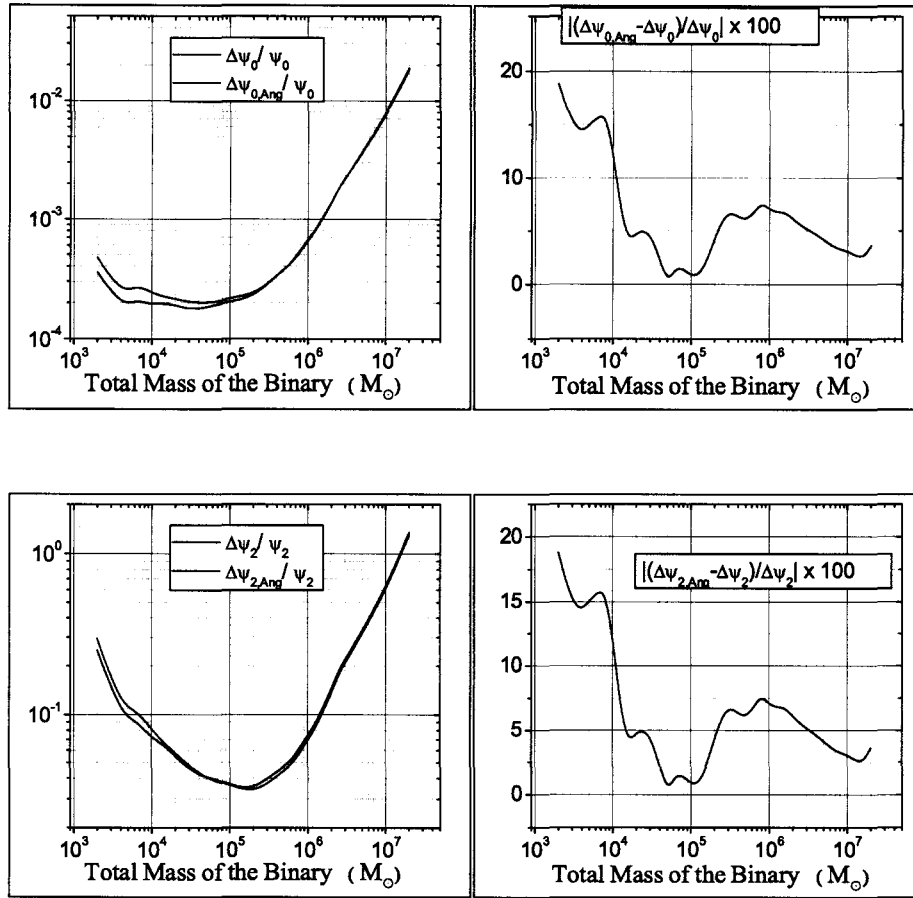


Figure 5.8: The left panels are the relative errors as a function of total mass of the binary. $\Delta\psi_k/\psi_k$ and $\Delta\psi_{kAng}/\psi_k$ are the relative errors in the cases with average orientation pattern and with orientation pattern respectively. The right panels are the percentage differences between the errors in the two cases relative to the error in the case of the average orientation pattern. The top panels corresponds to ψ_0 and the bottom panels corresponds to ψ_2 .

Chapter 5

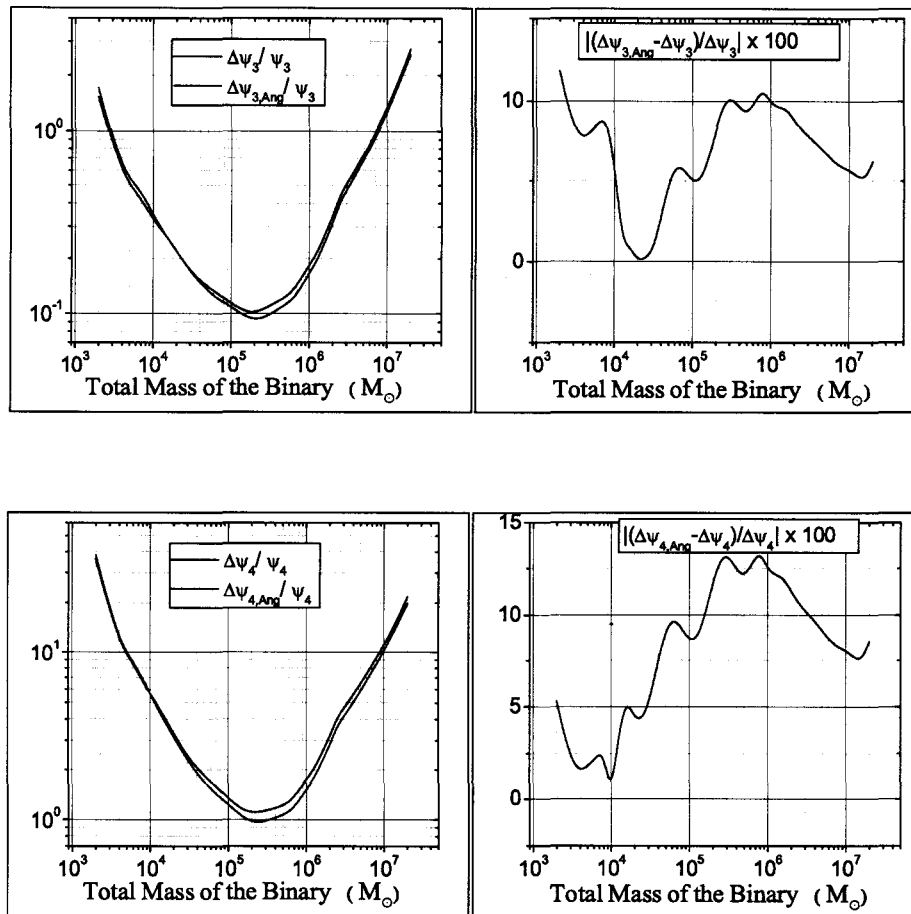


Figure 5.9: The left panels are the relative errors as a function of total mass of the binary. $\Delta\psi_k/\psi_k$ and $\Delta\psi_{k,Ang}/\psi_k$ are the relative errors in the cases with average orientation pattern and with orientation pattern respectively. The right panels are the percentage differences between the errors in the two cases relative to the error in the case of the average orientation pattern. The top panels corresponds to ψ_3 and the bottom panels corresponds to ψ_4 .

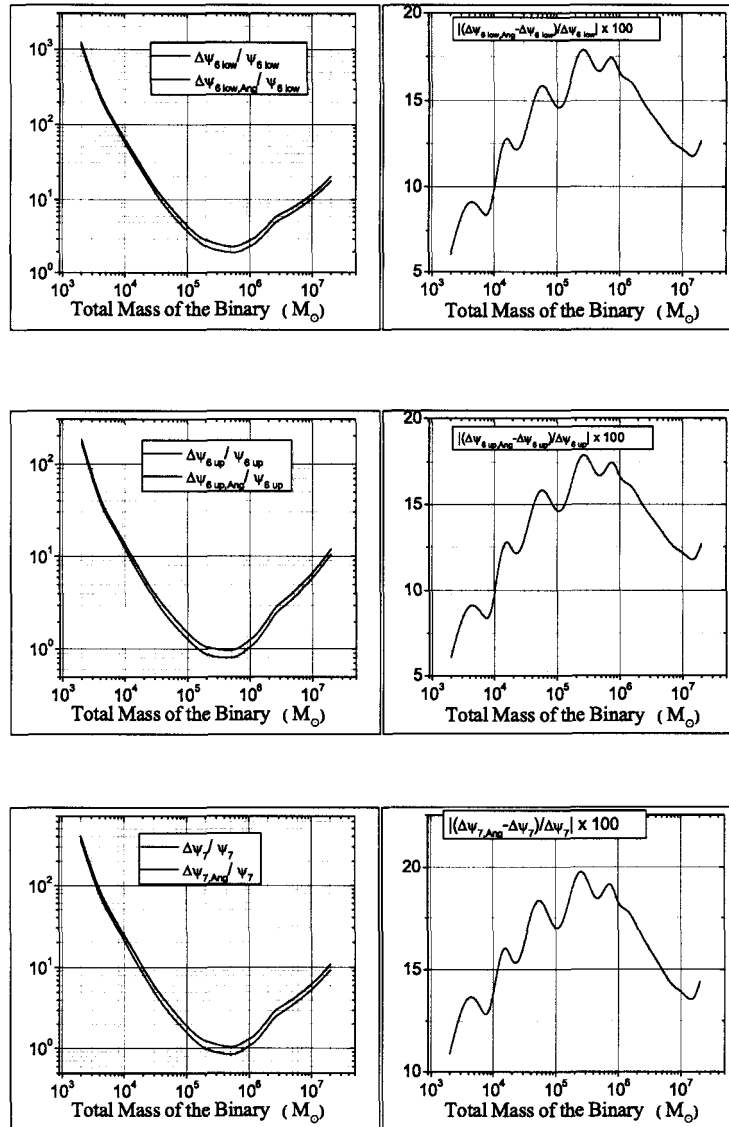


Figure 5.10: The left panels are the relative errors as a function of total mass of the binary. $\Delta\psi_k/\psi_k$ and $\Delta\psi_{k\text{ Ang}}/\psi_k$ are the relative errors in the cases with average orientation pattern and with orientation pattern respectively. The right panels are the percentage differences between the errors in the two cases relative to the error in the case of the average orientation pattern. The top panels corresponds to $\psi_{6\text{ low}}$ and the bottom panels corresponds to $\psi_{6\text{ up}}$.

could well be different for a different choice of orientation and parametrization [196, 210].

5.9.2 Test of general relativity: Representation in the m_1 - m_2 plane

A graphical plot in the m_1 - m_2 plane best illustrates how one might test the consistency of the individual masses of the specific system in the merger of black holes each of mass $10^{5.1}M_\odot$. We have chosen a system that gives the lowest errors in different parameters (cf. Fig. [5.7]) and assumed that the source is at a distance of 1 Gpc. For each parameter ψ_k we have plotted the region enclosed by the boundaries $\psi_k + \Delta\psi_k$ and $\psi_k - \Delta\psi_k$, where $\Delta\psi_k$ is the one-sigma error in the estimation of ψ_k . The region in the $m_1 - m_2$ plane for a binary of total mass M_0 corresponding to the parameter ψ_k is determined as follows. It is given by $R_k(m_1, m_2; (\psi_k)|_{M=M_0} - \delta_k) = 0$, where $-\Delta\psi_k|_{M=M_0} \leq \delta_k \leq \Delta\psi_k|_{M=M_0}$. (In the above $\Delta\psi_k$ corresponds to the estimated errors in ψ_k for a particular detector and particular source of total mass M_0 .)

In Fig. [5.11] the top-left panels correspond to the case where the log terms are treated as constants, the top-right panels to where the log terms are expanded and the bottom panels correspond to the case where the log terms are treated as independent parameters. The higher order ψ_k 's will have to enclose the region determined by, say ψ_0 and ψ_2 . This will be a stringent test for the various parameters and will be a powerful test if LISA sees a merger event with a high SNR of $\sim 10^4$. For binaries that merge within 1 Gpc the test would confirm the values of the known PN coefficients to within a fractional accuracy of ~ 1 .

Finally, one may wonder that there is no test corresponding to ψ_5 in Fig. [5.7] and Fig. [5.11]. The reason is simple. This term has no frequency dependence and consequently the associated constant ψ_5 gets absorbed into a redefinition of the coalescence phase Φ_c .

5.9.3 Bounds on Compton wavelength of the graviton using the current proposal

Based on the discussions of the previous section, it would be interesting to ask whether the proposed tests can, in principle, distinguish general relativity (GR) from, say a theory that also includes a massive graviton [195]. In this theory the 1PN parameter ψ_2 is different from that in GR [195]. The accuracy with which ψ_2 , which contains the massive graviton term, can be determined, can be used to put bounds on λ_g once we assume the additional term at this order is same as in Ref. [195].

We adopt the following procedure to calculate the bounds on the mass of graviton. The presence of the massive graviton modifies the 1PN terms of the phasing formula which can be conveniently rewritten as

$$\psi_2 = \psi_2^{\text{GR}} + \psi_2^{\text{MG}} \quad (5.51)$$

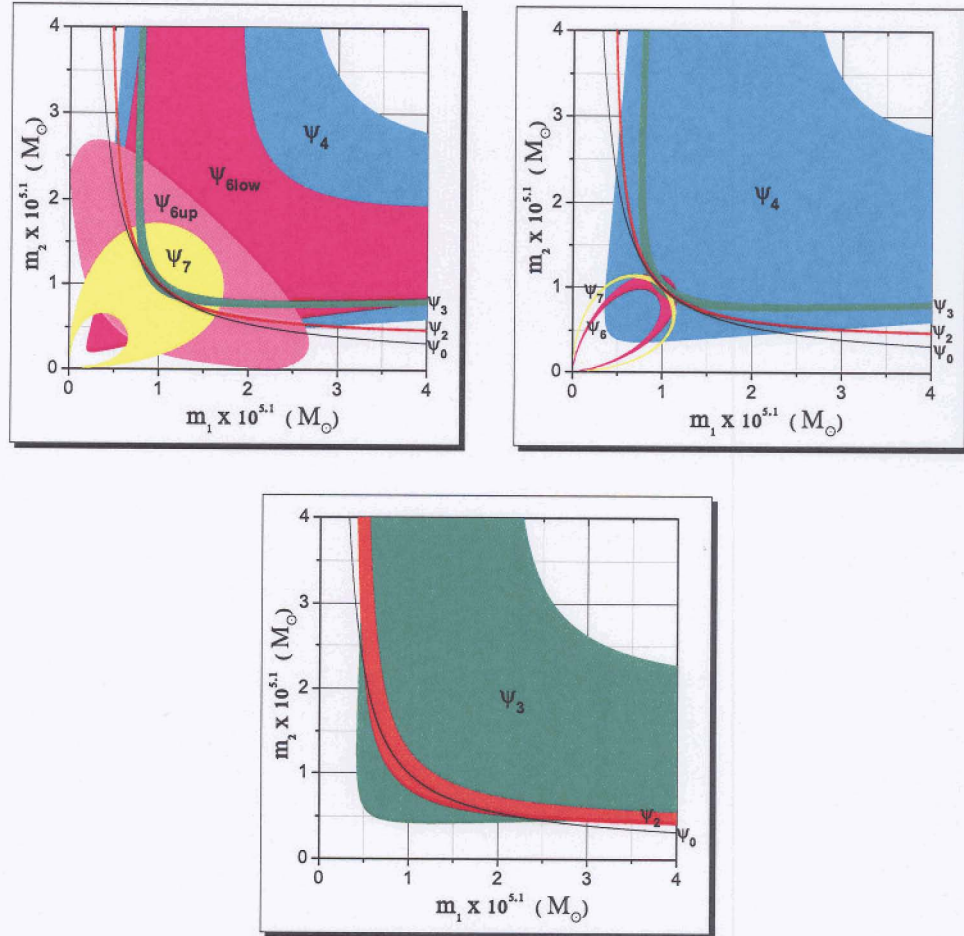


Figure 5.11: The m_1 - m_2 plane plots for different ψ_k 's for the three ways of dealing with log terms: **Top left** is the case where the log terms are treated as constants, the **top right** where the log terms are Taylor expanded about v_{iso} and retained to 3.5PN and the plot at the **bottom** refers to the case where the log terms are parameterized by independent variables. The source is assumed to be a binary BH of mass $M_0 = 2 \times 10^{5.1} M_\odot$, at a luminosity distance of 1000 Mpc for the LISA detector. The orientation of the source is chosen to be $(\cos \bar{\theta}_S, \bar{\phi}_S, \cos \bar{\theta}_L, \bar{\phi}_L) = (09, 2, -0.8, -5)$, an "optimal orientation". For each parameter ψ_k we have plotted the region enclosed by the boundaries $\psi_k + \Delta\psi_k$ and $\psi_k - \Delta\psi_k$, where $\Delta\psi_k$ is the one-sigma error in the estimation of ψ_k . A larger region means a weaker test and a less certain determination for m_1 and m_2 . The existence of a non-empty intersection for the regions associated with each ψ_k constitutes the test. In the last case, the plot includes only first three ψ_k 's since others are estimated with very large errors.

where

$$\psi_2^{\text{GR}} = \left(\frac{3715}{32256} + \frac{55}{384} \nu \right) \frac{1}{\pi \nu M} \quad (5.52)$$

and ψ_2^{MG} , the leading correction due to the effect of the massive graviton, is given by

$$\psi_2^{\text{MG}} = -\frac{c^2 \pi D}{(1+z)\lambda_g^2}. \quad (5.53)$$

ψ_2^{MG} will alter the arrival time of the waves of a given frequency and depends only on the size of the graviton Compton wavelength λ_g , and on the 'distance' D which is defined as [196, 195]

$$D = \frac{c(1+z)}{H_0} \int_0^z \frac{dz'}{(1+z')^2 [\Omega_M(1+z')^3 + \Omega_\Lambda]^{1/2}}. \quad (5.54)$$

It should be noted that D is not a conventional cosmological distance measure, like the luminosity distance D_L [195] and differs from it by a factor $(1+z^2)^{-2}$ in the integrand.

For a BH binary of total mass $2 \times 10^6 M_\odot$ at the luminosity distance $D_L = 3000$ Mpc, that is, ($z = 0.524116$ and $D = 2007.42$ Mpc) in the LISA band we find $\psi_2^{\text{GR}} = 0.0195$ and $\psi_2^{\text{MG}} \simeq -\frac{3.8}{(\lambda_g/(10^{14} \text{ km}))^2}$. From our results in the previous section 5.9.1 the error in estimating ψ_2 is $\Delta\psi_2 = \frac{446}{\rho(z)}$. Thus the massive graviton theory can be distinguished from GR if $\psi_2^{\text{MG}} \geq \Delta\psi_2$, say, $\psi_2^{\text{MG}} = 10 \times \Delta\psi_2$, which we choose as our criterion. For the system considered, one can then use the estimate of $\Delta\psi_2$ to obtain the value of λ_g , which satisfies this criterion. Any massive graviton theory of this type, with λ_g less than or equal to this value can be distinguished from GR by the proposed test.

Remarkably, we find that an year's worth of observation of BBH mergers in the mass range $2 \times 10^4 - 2 \times 10^7 M_\odot$ should be sufficient to discriminate GR from a massive graviton theory provided the Compton wavelength of graviton $\lambda_g \leq 5.5 \times 10^{14} - 3.8 \times 10^{15}$ kms. These limits make the simplifying assumption of neglecting the as yet uncomputed higher PN order corrections to GW phase in the massive graviton case. (See also [211] for a discussion regarding the extent to which GW observations can critically distinguish between different theories of gravitation in comparison to the binary pulsar tests.)

5.9.4 Summary and future directions

Let us begin with a tabular summary of the results of this chapter to highlight the main results. In Table 5.9.4 we summarise the minimum SNR required by the various ground-based detectors to test the various PN order coefficients with the proposed scheme (treating *all* PN coefficients as independent). From the table one can conclude that it will not be possible to test *any* of the PN coefficients ψ_k using the ground-based detectors. The situation in regard to LISA is similarly paraphrased in Table 5.9.4. In this case, at the generally

Table 5.1: This table lists the relative error $\Delta\psi_k/\psi_k$ for a prototypical binary black hole system each of $10M_\odot$ at a distance of 200 Mpc for the different ground-based detectors Virgo, Initial LIGO, Advanced LIGO and EGO. From the table it follows that the ground-based detectors cannot test any PN coefficient ψ_k , if *all* the ψ_k 's are treated as independent Parameters.

$M = 20M_\odot$ $D_L = 0.200$ Gpc				
	Virgo	Initial LIGO	Advanced LIGO	EGO
$\text{SNR} \equiv \rho$	1.92964	2.38892	37.5313	143.923
$\Delta\psi_0/\psi_0$	79.2489	577.437	4.53519	0.100777
$\Delta\psi_2/\psi_2$	4885.46	26954.9	274.267	8.11832
$\Delta\psi_3/\psi_3$	9282.07	45032.0	516.022	17.4466
$\Delta\psi_4/\psi_4$	69359.4	298013.	3818.32	146.395
$\Delta\psi_{6\text{low}}/\psi_{6\text{low}}$	50473.9	152923.	2725.24	152.228
$\Delta\psi_{6\text{up}}/\psi_{6\text{up}}$	34276.1	118037.	1850.67	89.2502
$\Delta\psi_7/\psi_7$	29953.6	93341.4	1602.03	85.6984

Table 5.2: This table summarizes the minimum values in the SNR required by LISA to test the PN coefficient ψ_k (more precisely at which the relative error $\Delta\psi_k/\psi_k \sim 1$) if *all* the ψ_k 's are treated independent. The last two columns give the associated maximum values of D_L in Gpc up to which this test is feasible. With a SNR of 1050, one can determine ψ_0, ψ_2 and ψ_3 using LISA.

$M = 2 \times 10^6 M_\odot$				
	LISA (Without pattern)	LISA (With pattern)	LISA (Without pattern)	LISA (With pattern)
	Minimum in $\text{SNR}=\rho$ to test ψ_k		Maximum in D_L (Gpc) to test ψ_k	
ψ_0	2.994523	4.593583	2145.462	2158.579
ψ_2	308.4470	446.7180	20.82898	22.19658
ψ_3	735.3999	1034.571	8.736249	9.584273
ψ_4	6760.243	9256.164	0.9503559	1.071244
$\psi_{6\text{low}}$	9941.631	12985.71	0.6462357	0.7635788
$\psi_{6\text{up}}$	4773.239	6234.780	1.345970	1.590370
ψ_7	4853.711	6214.063	1.323655	1.595673

Table 5.3: This table lists the SNR and fractional accuracies $\Delta\psi_k/\psi_k$ with which the PN coefficients ψ_k can be tested by LISA using a prototypical supermassive binary black hole system ($2 \times 10^6 M_\odot$) at three representative distances of 1 Gpc, 3 Gpc and 6.6122 Gpc ($z = 1$). From the table it follows that, if all the PN coefficients are treated as independent parameters, only ψ_0 , ψ_2 and ψ_3 can be tested at all the three distances. ψ_7 can be tested only if the source is relatively closer at $D_L = 1$ Gpc.

	LISA $M = 2 \times 10^6 M_\odot$					
	$D_L = 1$ Gpc		$D_L = 3$ Gpc		$D_L = 6.6122$ Gpc	
	(Without pattern)	(With pattern)	(Without pattern)	(With pattern)	(Without pattern)	(With pattern)
SNR $\equiv p$	6424.64	9915.61	2141.55	3305.2	971.629	1499.59
$\Delta\psi_0/\psi_0$	0.000466100	0.000463268	0.00139830	0.00138980	0.00308196	0.00306323
$\Delta\psi_2/\psi_2$	0.0480100	0.0450520	0.144030	0.135156	0.317453	0.297894
$\Delta\psi_3/\psi_3$	0.114466	0.104338	0.343397	0.313013	0.756873	0.689904
$\Delta\psi_4/\psi_4$	1.05224	0.933494	3.15671	2.80048	6.95764	6.17248
$\Delta\psi_{6\text{low}}/\psi_{6\text{low}}$	1.54742	1.30962	4.64227	3.92887	10.2319	8.65953
$\Delta\psi_{6\text{up}}/\psi_{6\text{up}}$	0.742959	0.628784	2.22888	1.88635	4.91262	4.15767
$\Delta\psi_7/\psi_7$	0.755484	0.626695	2.26645	1.88008	4.99544	4.14385

realistic **SNR** of about **1050 LISA** can test for ψ_0 , ψ_2 and ψ_3 . The last two columns of this Table 5.9.4 on the other hand provides a similar comparison in terms of the maximum luminosity distance to which the **LISA** detector can test a particular **PN** coefficient. Finally, in Table 5.9.4, for the case of **LISA** we provide a ready-reckoner of the relative errors in various **PN** parameters ψ_k for a prototypical supermassive binary black hole ($2 \times 10^6 M_\odot$) at three typical distances.

Let us finally conclude with the limitations of the present work and an indication of the possible directions in which the results can be extended.

- In the present work we have dealt with only non-spinning binaries. The spin parameters, β from spin-orbit coupling at 1.5PN and σ from spin-spin coupling at 2PN, are assumed to be less significant for these equal mass systems. For the unequal mass case the spin effects are expected to be more important.
- Orbital eccentricity, which might introduce systematic effects in these tests, has not been included as we have restricted our analysis to binaries in quasi-circular orbits. Especially for many **LISA** sources the binaries could be in quasi-eccentric orbits and thus require an extension to include eccentricity.
 - a Massive graviton theories can be tested since they lead to a phasing formula that is structurally similar to general relativity but with terms modified due to the propagation delay. Further work would eventually require the computation of higher **PN** order effects in such theories beyond the lowest order effect considered usually including the present work.
 - a Alternative theories of gravity, such as the Brans-Dicke theory, where the **PN** structure of the phasing is different due to the presence of dipolar radiation, may also be tested by an extension of the above proposal.

These and other issues should be investigated in the future.

5.10 Appendix

5.10.1 Effect of increasing dimensionality on parameter estimation due to inclusion of higher post Newtonian terms

In this Appendix we study the effect of increasing dimensionality caused due to the inclusion of higher PN order terms as independent parameters on the errors in the estimation of ψ_k s. For this, we estimated the errors, say in ψ_0 , when the signal is progressively more accurate starting from Newtonian, 1PN, ... to 3.5PN. A similar exercise is repeated for other ψ_k 's also and the results for the Advanced LIGO, EGO and LISA detectors are presented below. One should bear in mind that systematic errors due to the neglect of higher orders will be dominant in many cases. The increase in dimensionality degrades the accuracy of determinations of a particular ψ_k , as one would expect. For simplicity the log terms are treated as constants.

For each detector, Advanced LIGO (Fig [5.12]), EGO (Fig [5.13]) and LISA (Fig [5.14]) there are five panels corresponding to the relative errors of ψ_0 , ψ_2 , ψ_3 , ψ_4 and $\{\psi_{6,\text{low}}$ and $\psi_{6,\text{up}}\}$ respectively. In each panel the test is performed successively with progressively more accurate PN waveforms. Increased dimensionality of the parameter space leads to a poorer determination of a particular PN coefficient if **all** the PN coefficients are treated as independent parameters.

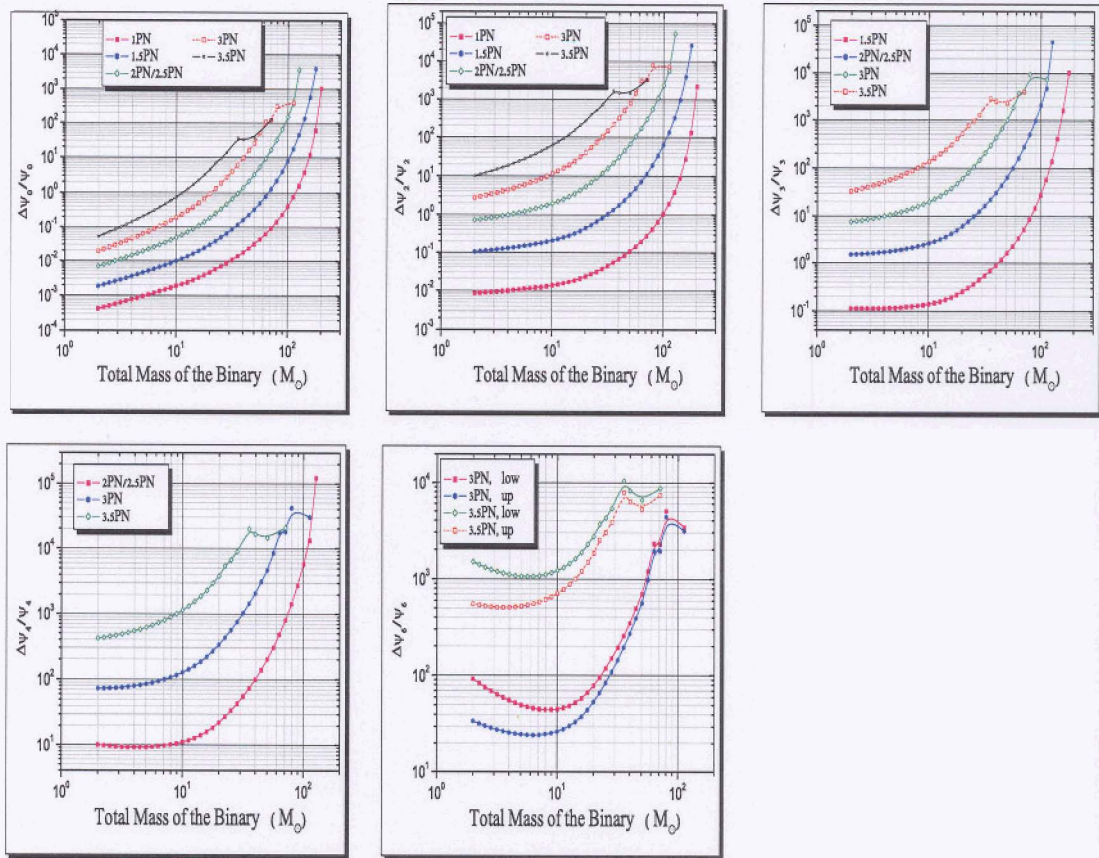


Figure 5.12: Effect of increasing dimensionality on parameter estimation due to inclusion of higher post Newtonian terms as independent parameters for the Advanced-LIGO Detector.

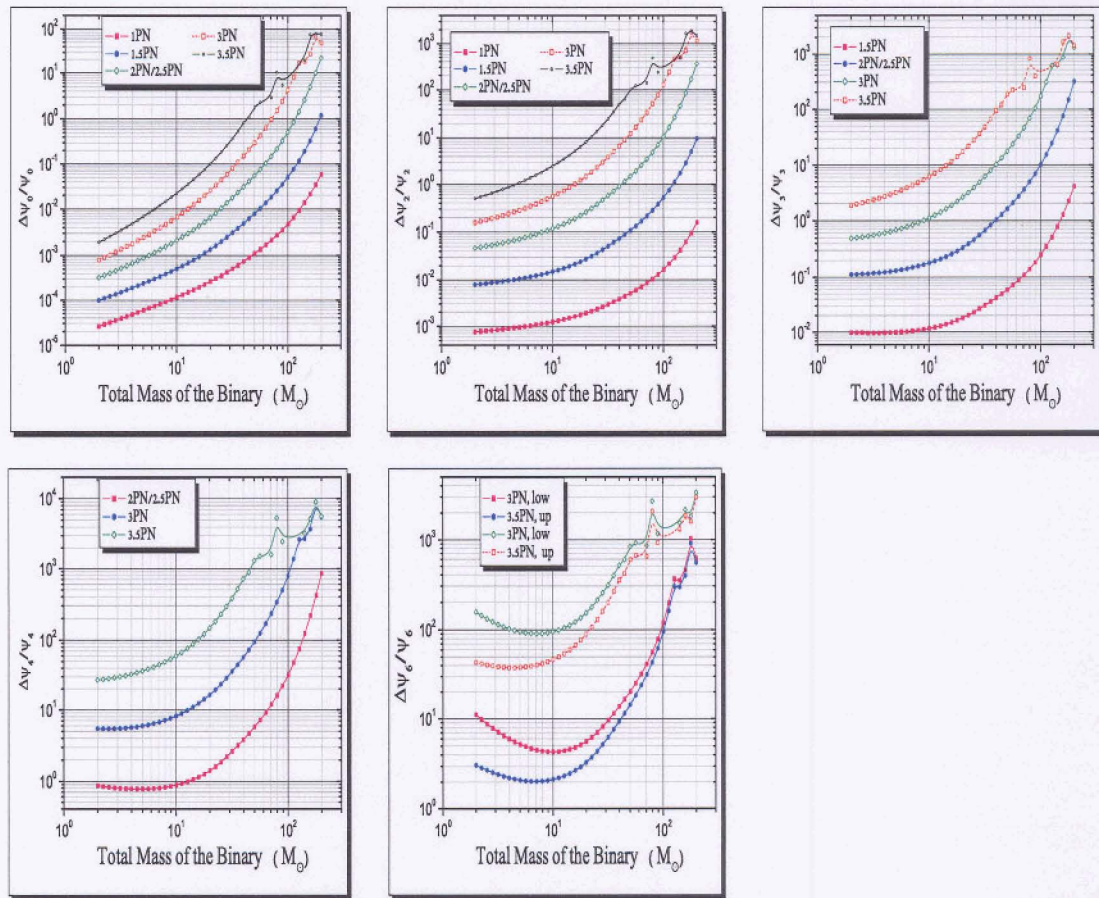


Figure 5.13: Effect of increasing dimensionality on parameter estimation due to inclusion of higher post Newtonian terms as independent parameters for the EGO Detector

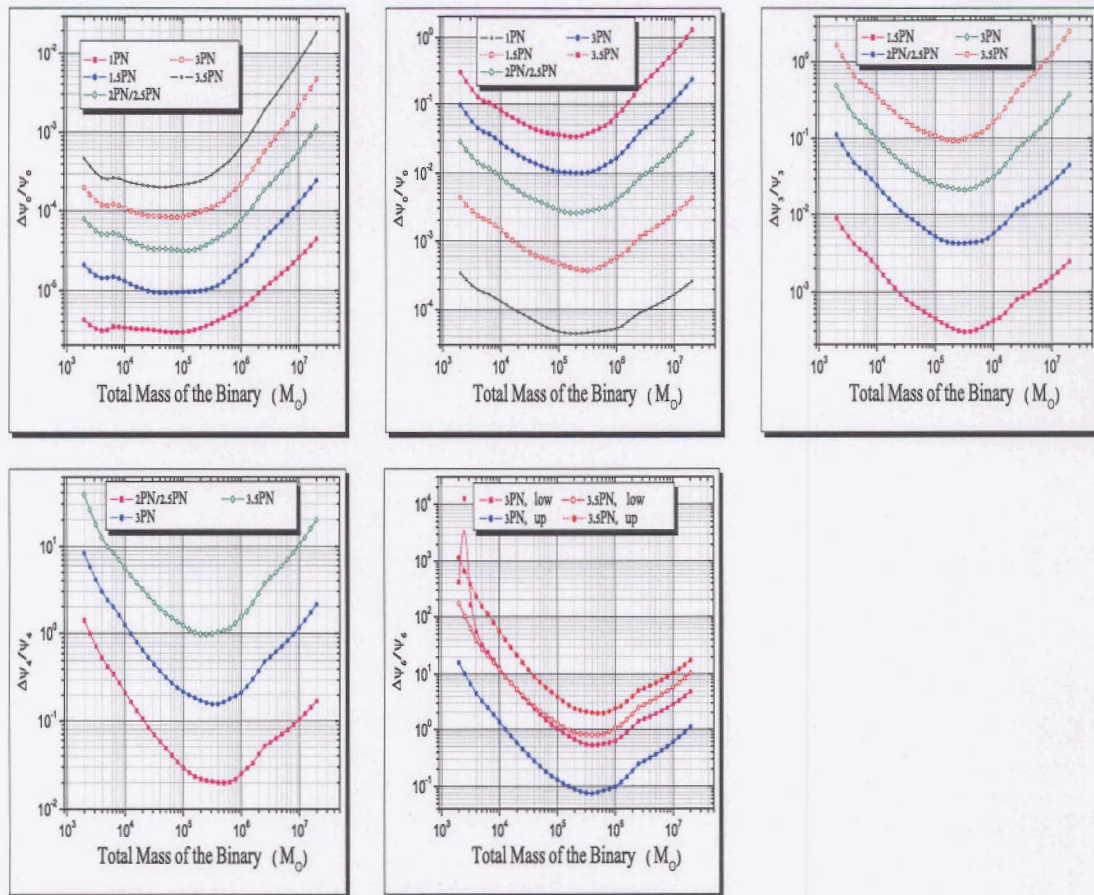


Figure 5.14: Effect of increasing dimensionality on parameter estimation due to inclusion of higher post Newtonian terms as independent parameters for the LISA Detector